ACOUSTICALLY ENHANCED BOILING HEAT TRANSFER

A Thesis
Presented to
The Academic Faculty

By

Zachary W. Douglas

In Partial Fulfillment
Of the Requirements for the Degree
Master of Science in Mechanical Engineering

Georgia Institute of Technology

August, 2007

ACOUSTICALLY ENHANCED BOILING HEAT TRANSFER

Approved by:

Dr. Ari Glezer
School of Mechanical Engineering
Georgia Institute of Technology

Dr. Marc K. Smith
School of Mechanical Engineering
Georgia Institute of Technology

Dr. G. Paul Neitzel
School of Mechanical Engineering
Georgia Institute of Technology

Date Approved: July 9, 2007

ACKNOWLDEGMENTS

First and foremost, I would like to express my sincere thanks to my wife and my parents. Their love and support has made the good times better and the bad times bearable. I appreciate them for all of their encouragement and for always listening to my rants and raves.

In addition, I would like to thank my advisors, Dr. Ari Glezer and Dr. Marc K. Smith. This project could not have been completed without their leadership, insight, and guidance. I would also like to thank the third member of my reading committee, Dr. G. Paul Neitzel. A special thank you is also due to Dr. Samuel Heffington for his help on the project and to Dr. Peter Hesketh for his help in electroplating the single bubble heater. I would also like to express my gratitude to John Graham and Vladimir Bortkevich from the ME machine and electronics shops, respectively, for their work in fabricating the experimental setup. The work was supported by the NASA Microgravity Research Program under Grant NAG3-2763 and the Woodruff Foundation.

Last, but not least, I would like to thank the other members of the lab and my other friends at Georgia Tech for their innumerable research consultations and extracurricular entertainment.

TABLE OF CONTENTS

LIST OF TABLES

LIST OF FIGURES

NOMENCLATURE

A	cross-sectional area, (m^2)
a	dummy variable representing radial position, (m)
AC	alternating current
CHF	critical heat flux, (W/cm^2)
c_ℓ	specific heat of a liquid, (kJ/kgK)
D	bubble diameter, (m or mm)
d	separation distance, (m, cm, or mm)
f	frequency, (Hz or kHz)
f_b	frequency of bubble liftoffs, (Hz)
F_B	buoyant force, (N)
F_{B1}	primary Bjerknes force, (N)
F_{B2}	secondary Bjerknes force, (N)
f_D	driving frequency of acoustic driver, (Hz or kHz)
f(L')	geometry specific function of L′
fps	frames per second
F_r	vapor recoil force, (N)
g	acceleration of gravity, (m/s^2)
h_{fg}	latent heat of vaporization, (kJ/kg)
$\overline{h_{nc}}$	average natural convection coefficient, (W/m^2K)
K	ratio of the surface area influenced by a bubble to the projected area of the bubble on the surface
k	wave number

k_{Cu}	thermal conductivity of copper, (W/mK)
k_ℓ	thermal conductivity of a liquid, (W/mK)
L	characteristic length, (m)
L'	dimensionless characteristic length
N_a	nucleation site density, (sites/m^2)
P	pressure, (Pa or kPa)
p	diameter of the copper pin, (mm)
P_a	sound pressure amplitude, (Pa or kPa)
P_0	static pressure, (Pa or kPa)
Q	heat, (W)
q''	heat flux, (W/cm^2)
q''_{CHF}	critical heat flux, (W/cm^2)
$q''_{CHF,SAT}$	critical heat flux at saturated conditions, (W/cm^2)
$q''_{CHF,SUB}$	critical heat flux at subcooled conditions, (W/cm^2)
$(q'')^*$	maximum device heat flux, (W/cm^2)
R	radius of piezoelectric diaphragm free to oscillate, (m or mm)
r	radial distance from center of piezoelectric diaphragm, (m or mm)
r'	distance from a point (r, z) to a differential area on the piezoelectric diaphragm, (m)
r''	distance from a point (r, z) to a differential area on the image piezoelectric diaphragm, (m)
R_0	equilibrium radius of a bubble, (m or mm)
R_{01}	equilibrium radius of first bubble, (m or mm)
R_{02}	equilibrium radius of second bubble, (m or mm)

r_{12}	distance between two bubble's centers, (m, cm, or mm)
R_b	departure radius of a bubble, (m or mm)
T	temperature, (°C)
T_c	characteristic time, (s)
t	time, (s)
T_{Cu}	copper temperature, (°C)
T_S	surface temperature, (°C)
$(T_S)^*$	maximum allowable device temperature, (°C)
T_{SAT}	saturation temperature, (°C)
T_{SS}	stainless steel temperature, (°C)
T_{SUB}	bulk temperature of subcooled liquid, (°C)
V	volume, (m^3)
V_a	time periodic volume amplitude, (m^3)
V_D	driving voltage of acoustic driver (rms unless otherwise noted), (V)
$\overline{V_{ME}}$	average volume of the microlayer, (m^3)
V_{pp}	peak-to-peak voltage, (V)
V_{rms}	root mean square voltage, (V)
x	distance, (m)
z	axial distance from piezoelectric diaphragm, (cm)

Greek

α	nondimensional constant
β	contact angle, (radians or degrees)

δR	radial oscillation of a single bubble, (m, mm, or μm)
δR_1	radial oscillation of first bubble, (m or mm)
δR_2	radial oscillation of second bubble, (m or mm)
η	evaporation rate, (kg/m^{2}s)
θ	dummy variable representing azimuthal position, (radians)
κ	polytropic exponent
λ	wavelength, (m or mm)
ξ	distance from nearest pressure node, (m)
ρ_g	gas density, (kg/m^3)
ρ_ℓ	liquid density, (kg/m^3)
ρ_v	vapor density, (kg/m^3)
σ	surface tension, (N/m)
φ	phase difference, (radians or degrees)
ϕ	surface orientation, (radians or degrees)
Ψ_0	constant, (Pa/m)
ω	angular frequency, (rad/s)
ω_0	resonance frequency of a bubble, (Hz or kHz)

Other

$\langle\ \rangle$	time average

SUMMARY

The work performed and presented in this thesis explores the efficacy of using a small, lightweight, low-power acoustic driver to enhance boiling heat transfer from a flat surface by forcibly removing vapor bubbles from the surface and inhibiting the instabilities responsible for the transition to film boiling at the critical heat flux. The acoustic field produced by the acoustic driver induces interfacial instabilities that affect the bubble's contact line with the surface and result in bubble detachment from the heated surface. Once detached, the bubble can easily be advected into the bulk liquid by acoustic, buoyant, or other forces.

In order to characterize the effects of the acoustic field produced by the acoustic driver on a bubble, individual air and vapor bubbles in the presence of the acoustic field are studied. Variables contributing to the presence and magnitude of interfacial instabilities are the frequency and sound pressure amplitude of the acoustic field and the bubble diameter. The effects of the acoustic field on a single vapor bubble are studied using a novel, flat boiling heat transfer surface designed to produce a single vapor bubble of a prescribed size. After a vapor bubble has been detached from the heated surface, the bubble hovers on a thin layer of liquid near the surface due to an acoustic force that overcomes the upward pull of the buoyant force. Experiments show that the acoustic force is not a result of bulk fluid movement or acoustic streaming. Instead, this force is attributed to the secondary Bjerknes force, which is typically thought of as the force between two oscillating gas bubbles in an acoustic field, but has also been shown to act on a single oscillating bubble in the vicinity of a rigid wall (Hao, Oguz et al. 2001).

Next, the effect of the acoustic field on the boiling process from a 1 cm^2 horizontal copper heater is studied. Acoustic enhancement using the acoustic driver is shown to increase the pool boiling critical heat flux (CHF) from 333 W/cm^2 (T_S - T_{SAT} = 40.1°C) to 446 W/cm^2 (T_S - T_{SAT} = 49.7°C) at 19.8°C subcooling, an increase of 34%. The acoustic field limited the formation of large vapor columns and delayed the transition from nucleate to film boiling. The acoustic enhancement is observed at acoustic frequencies between 0.7 and 1.2 kHz. It is possible that frequencies lower than 0.7 kHz could show a similar improvement, but these frequencies are not tested due to limitations on the acoustic driver. Frequencies above 1.2 kHz are thought to be too large to adequately influence the vapor structures on a 1 cm^2 heater. Preliminary experiments using a heater with a smaller exposed surface indicate that larger frequencies would be effective on a smaller heater.

When the distance between the boiling surface and the acoustic driver is less than 1 cm, a vapor bridge forms between the two and serves to decrease the CHF. At a separation distance of only 3.5 mm the natural CHF decreases to 165 W/cm^2. At the same separation distance, the acoustically enhanced CHF decreases to only 338 W/cm^2, now representing a 147% improvement. When engineering requirements constrain a boiling surface to be very near a wall, the acoustic enhancement described in this work could prove beneficial in increasing the CHF from the boiling surface to an appropriate level.

CHAPTER 1

INTRODUCTION

Advances in the microelectronics industry have led to increasingly smaller and faster electronic integrated circuits. The reduction in size and increase in speed have resulted in an increase in heat generation, and with it, the need for improved heat removal. In older or less sophisticated systems, cooling is generally accomplished using natural or forced air convection. Typically these systems are only capable of heat removal on the order of 10 W/cm^2 (Sellers 2000). Since heat fluxes from modern integrated circuits are projected to exceed 1000 W/cm^2 in the next five to ten years (Zerby and Kuszewski 2002), new methods for electronic cooling have been developed, such as liquid convection and two-phase cooling (Bar-Cohen 1993; Mudawar 2000).

Liquid cooling methods are used because liquids tend to have a much greater thermal conductivity than gas, so natural and forced convection are enhanced. Two-phase cooling in the form of boiling also utilizes the constant temperature heat absorption by a fluid undergoing a liquid-to-gas phase change to remove additional heat from the cooled hardware. In addition, the process of vapor bubbles forming on the hot surface and then moving into the bulk liquid results in fluid movement which further increases convection. However, boiling heat transfer is limited by the critical heat flux. If this maximum heat flux limit is exceeded, an insulating vapor film will cover the entire heat transfer surface resulting in a dramatic increase in the surface temperature and possible severe damage to the cooled hardware.

Research into enhanced boiling seeks to improve the heat transfer from a surface at a given surface temperature or extend the critical heat flux limit. One method for doing this is to facilitate better removal of the vapor bubbles from the heated surface. Simply, this can be done by using a pump to move the coolant through the system and remove the bubbles from the surface because of the resulting drag. However, this comes at a severe cost in power, weight and size of the system (Agostini, Fabbri et al. 2007). Research at Georgia Tech has focused on the use of small, lightweight, low-power acoustic drivers to remove vapor bubbles from a surface by the creation of either a synthetic jet (Heffington, Tillery et al. 2003; Tillery, Heffington et al. 2004; Tillery, Heffington et al. 2006) or pressure waves (Heffington and Glezer 2004).

The current research aims to remove vapor bubbles from a heated surface using the interactions between a vapor bubble and an acoustic field induced by an acoustic driver. The effects of the acoustic field can be in the form of volume or radial oscillations, surface waves, and the resulting net forces. It is hypothesized that these effects can allow the use of an acoustic field to change the natural boiling process in such a way that the boiling curve is shifted or the critical heat flux increased. In the experiments described here a small, lightweight, low-power acoustic driver is used to create an acoustic field. The effect of this acoustic field on vapor bubbles and the boiling process is then studied.

The results can best be described in two primary categories. The first category, described in Chapter 5, consists of those experiments for which the purpose is to determine the effect of the sound field produced by the acoustic driver on a single bubble. In each case efforts are made to isolate a single bubble of a desired size for study. The

second category, described in Chapter 6, consists of those experiments performed with a calibrated copper heater for the purpose of making heat flux measurements. The same acoustic driver is used to alter the natural boiling process from the heater's surface. In these cases, no effort is made to isolate a single vapor bubble, and often the concept of a single bubble does not exist as high heat fluxes result in the formation of vapor columns and other more complex structures. The results of experiments from this category are often more global in nature and reflect the acoustics' overall effect on the heat flux, not the effect on a single bubble.

1.1 Background

1.1.1 Boiling

Boiling is often described using the standard boiling curve shown in Figure 1 (Tillery 2004). The horizontal axis represents the difference between the surface temperature and the saturation temperature of the fluid, known as wall superheat, while the vertical axis represents the wall heat flux.

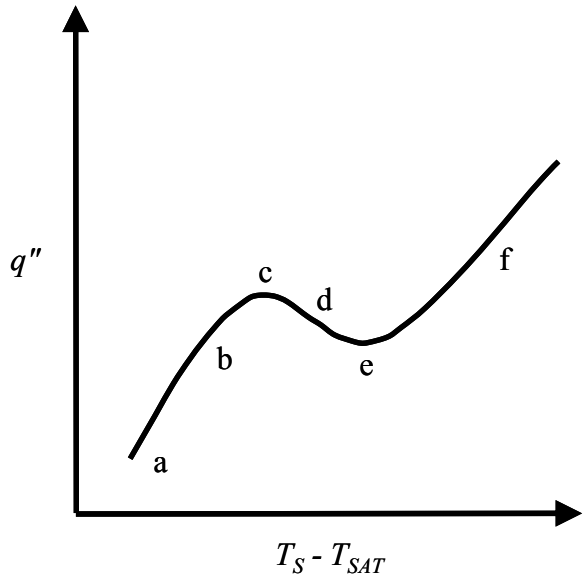

Figure 1. The standard boiling curve. Regimes: a) natural convection, b) nucleate boiling, c) critical heat flux, d) transition boiling, e) minimum heat flux limit, f) film boiling.

At wall temperatures below the saturation temperature of the liquid, and even slightly above it, the heat transfer is accomplished by natural convection (regime a in Figure 1). Once the wall superheat is sufficiently high to overcome the surface energy associated with a vapor-liquid interface (Wang and Dhir 1993), small bubbles begin to form, grow, and depart from the nucleation sites on the surface. Nucleation sites are small cracks or cavities on the surface where air or vapor is trapped. This is known as nucleate boiling and is shown as regime b in Figure 1. As the heat flux continues to increase, the bubbles grow larger and may even merge with other bubbles from the same nucleation site that have already detached from the surface, but have not yet been advected away, to form vapor columns. Adjacent columns may also merge above the surface to form vapor structures that resemble a mushroom with multiple stems or a tooth with multiple roots (Dhir 1998). At point c in Figure 1 the surface becomes completely crowded with vapor bubbles and columns. This point is known as the critical heat flux (CHF). When the heat

flux is increased from here, the vapor bubbles covering the surface act as an insulator, resulting in an increase in surface temperature system rapidly transitions to the film boiling regime (shown as f in Figure 1). The transition from c to f on the curve is very rapid and the surface temperature increase can be quite dramatic, often exceeding the melting temperature of the heater. Due to the speed with which a boiling surface passes through the transition regime, the CHF and the transition to film boiling are not well understood.

When the critical heat flux is reached, the rapid increase in surface temperature often leads to a catastrophic failure of electronic devices that are cooled by boiling heat transfer. Therefore, research on enhanced boiling seeks to increase the critical heat flux and decrease the associated surface temperature as shown schematically in Figure 2, which is a slightly modified version of a figure from Mudawar and Anderson (1989).

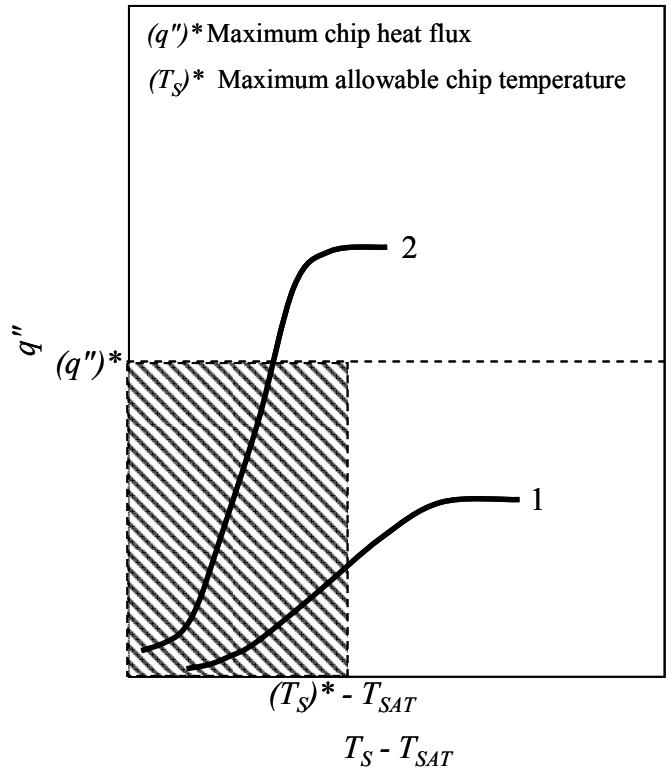

Figure 2. Graph of heat flux, q'', versus wall superheat, $T_S - T_{SAT}$, illustrating the goals of enhanced boiling in electronic cooling, i.e, going from curve 1 to curve 2.

The maximum heat generated by a given device is $(q'')^*$ and the maximum temperature that it can sustain is $(T_S)^*$. For a typical boiling curve (curve 1 in Figure 2), the CHF is below $(q'')^*$ and above $(T_S)^*$. In other words, the device produces more heat than can be removed by the boiling process, resulting in failure. In order to prevent such failure, enhanced boiling must increase the CHF above $(q'')^*$ while the surface temperature remains below $(T_S)^*$ (curve 2 in Figure 2).

Enhanced boiling methods can be either active or passive. Passive methods require no external power input and often involve surface modifications to increase the efficiency at which heat is removed from the surface, e.g., (Gaertner 1967; Webb 1981; Takata, Hidaka et al. 2003; Wen and Ho 2003). Active methods, like the method in this

research, require an external power input and often involve removal of vapor bubbles from the boiling surface to increase the heat transfer and delay the onset of film boiling, e.g., (Wong and Chon 1969; Park and Bergles 1988; Heffington and Glezer 2004; Ho-Young, Yi Gu et al. 2004; Tillery, Heffington et al. 2006; Agostini, Fabbri et al. 2007).

One can see that effective active and passive enhanced boiling methods could have many possible applications. Active methods, in particular, also have applications in microgravity boiling environments. In un-enhanced boiling, vapor is advected from the vicinity of the surface by buoyancy. Since the buoyancy force scales with the acceleration of gravity, it is negligible in a microgravity environment. Without this force, vapor quickly builds up on the vicinity of the surface until the entire surface is blanketed with the vapor. The CHF can be drastically decreased (Straub 2005). Enhanced boiling that utilizes other forces to remove vapor bubbles from the boiling surface can be used as a substitute for the buoyant force, thereby making boiling heat transfer cooling in a microgravity environment a more feasible proposition.

1.1.2 Gas Bubbles in an Acoustic Field

The intent of this research is to exploit the interactions between a bubble and a sound field to remove vapor bubbles from a boiling surface. When a gas bubble is in the presence of an acoustic field it undergoes radial oscillations due to the time-dependent pressure field. The frequency of these oscillations is equal to the frequency of the acoustic field, though the relative phase of the oscillations is dependent on the resonance frequency of the bubble. The resonance frequency of a spherical gas bubble is a function

of the bubble's size, the static pressure, and fluid properties as shown in Equation 1 (Leighton 1994).

$$\omega_0^2 = \frac{3\kappa P_0}{\rho_\ell R_0^2} + \frac{2\sigma}{\rho_\ell R_0^3}(3\kappa - 1) \tag{1}$$

where ω_0 is the resonance frequency, κ is the polytropic exponent, P_0 is the static pressure, ρ_ℓ is the liquid density, R_0 is the equilibrium radius, and σ is the surface tension. The surface tension term scales with $1/R_0^3$, while the static pressure term scales with $1/R_0^2$. For saturated water under atmospheric pressure, the surface tension term contributes less than 1% to the total for bubbles with R_0 > O(100 μm) and is often neglected. When a bubble is driven by an acoustic field of a frequency less than its resonance frequency, the bubble's oscillations are in phase with the driving frequency (i.e. the volume has a minimum at maximum pressure). However, if the driving frequency is larger than the resonance frequency, the bubble's oscillations are 180° degrees out of phase with the driving signal. Leighton (1994) explains this phenomena by modeling the bubble as a forced undamped oscillator.

The radial oscillations of the bubble and the changing pressure field result in a net force on the bubble known as the radiation force or primary Bjerknes force (Bjerknes 1906). For a general bubble this force is proportional to the time averaged product of the volume of the bubble and the gradient of the pressure field (Leighton 1994). In a standing acoustic wave the primary Bjerknes force on a spherical gas bubble is

$$F_{B1} = \frac{2\pi^2 R_0^3 P_a^2}{3P_0 \lambda \kappa \left(1 - \frac{\omega^2}{\omega_0^2}\right)} \sin\left(\frac{4\pi\xi}{\lambda}\right) \tag{2}$$

where P_a is the pressure amplitude of the standing wave, ξ is the distance from the nearest pressure node, and λ and ω are the wavelength and frequency, respectively, of the standing wave (Eller 1968; Sitter, Snyder et al. 1998b). When the driving frequency is larger than the bubble's resonance frequency, ω_0, the direction of the primary Bjerknes force is towards the nearest pressure node (z can never be larger than $\lambda/4$). However, when the driving frequency is less than the bubble's resonance frequency the force is directed towards the nearest pressure antinode. In a standing wave, a pressure antinode is always located at the reflecting wall, so bubbles with a resonance frequency larger than the frequency of the standing wave are forced towards the wall by the primary Bjerknes force.

When two bubbles are in close proximity to each other in a sound field, their radial oscillations induce a force between the bubbles (Barbat, Ashgriz et al. 1999) (known as the secondary Bjerknes force) which, can be either attractive or repulsive depending on the relative phases of the bubbles. The secondary Bjerknes force between two spherical bubbles is

$$F_{B2} = -\frac{2\pi\rho_\ell \omega^2 R_{01}^2 R_{02}^2}{r_{12}^2} (\delta R_1)(\delta R_2) \cos\varphi \tag{3}$$

where R_{01} and R_{02} are the equilibrium radii of the two bubbles, δR_1 and δR_2 are the respective radial oscillations, r is the distance between the two bubble's centers, ω is the driving frequency, and φ is the phase difference between the two bubbles' radial oscillations (a negative force represents an attractive force between the two bubbles) (Crum 1975). If both bubbles are either larger or smaller than the resonance size, then the phase difference becomes zero and the force is attractive. When one bubble is larger and the other bubble is smaller than the resonance size the phase difference approaches 180° and the force is repulsive.

When a single bubble is oscillating due to a time-dependent pressure field in the vicinity of a rigid wall, and if the flow can be assumed to be potential (inviscid and irrotational), the effect of the wall can be modeled as an image bubble of equal size at equal distance on the opposite side of the wall's surface (Hao, Oguz et al. 2001). The image bubble is equal in every way to the real bubble, so its oscillations are in phase with the real bubble, and therefore the real bubble is always attracted towards the wall.

Capillary waves have been observed on the surface of a gas bubble in an acoustic field (Koster and Sani 1990; Holt and Trinh 1996). A capillary wave is a small wave on the interface between two fluids for which the dominant restorative force is surface tension (i.e., gravity is negligible). The restorative force pulls the interface back towards its equilibrium location after a disturbance has passed. When one fluid is much denser than the other fluid (as is the case with a liquid-gas interface), then $\rho_\ell - \rho_g \approx \rho_\ell$, and the wavelength, λ, and the frequency, f, of a capillary wave are related by Equation 4 (Lighthill 1978).

$$f^2 = 2\pi \frac{\sigma}{\rho_\ell \lambda^3} + \frac{g}{2\pi\lambda} \tag{4}$$

where σ and ρ_ℓ are the surface tension and liquid density respectively. In order for the assumption that gravity is negligible to hold, the wavelength must be small ($\lambda < 4$ mm for 97% accuracy on a water-air interface at standard conditions). For larger waves, gravity becomes the dominant restorative force.

The current research utilizes an acoustic field to induce capillary waves on the surface of bubble. The waves are made large enough to result in detachment of the bubble from the surface. Once detached from the surface, the acoustic forces can more easily advect the bubble into the bulk liquid to allow for cooler liquid to take its place and improve the heat transfer from the boiling surface. The result is an increased critical heat flux due to the acoustic enhancement.

CHAPTER 2

LITERATURE REVIEW

Systematic studies of boiling began in earnest during the mid 1950's. The latent heat capacity of a liquid and the lack of a thermal contact resistance at a fluid-solid interface make boiling an attractive heat transfer option. The explosion of electronic devices of ever increasing power and decreasing size over the same time period has continually created a need for increasingly effective means of cooling. The history of liquid cooling of electronics was reviewed by Bar-Cohen (1991). However, as discussed in Chapter 1 above, the boiling heat transfer approach is limited by the critical heat flux (CHF). In efforts to increase the effectiveness of boiling heat transfer, methods for overcoming this limit are sought. An attractive approach for improving boiling heat transfer (and the one investigated here) is the manipulation of vapor bubbles using an acoustic field. This section begins by reviewing literature on the characteristics of the pool boiling process, including predictions of the CHF and the physical phenomena thought responsible for the transition from nucleate boiling to film boiling. Then, literature on the development of both active and passive techniques for enhancing pool boiling heat transfer is covered. Next, because the current approach involves the manipulation of vapor bubbles using an acoustic field, research on the behavior of bubbles in such a field is discussed. Finally, the research on methods for using an acoustic field to enhance the boiling process is reviewed.

2.1 Boiling

Boiling is useful as a means of cooling because of the large amount of heat absorbed by a fluid in the transition from a liquid to a gas. The pool boiling process is reviewed by Dhir (1991; 1998). Due to the complicated fluid mechanics and thermodynamics involved, the exact behavior of a boiling surface has proved difficult to predict mechanistically (Dhir 2006) or to model numerically (Dhir 2001), but many researchers have created models or correlations to predict the amount of heat transfer or the value of the critical heat flux (CHF) for a boiling process based on fluid properties, surface geometry, and measurable quantities (e.g., surface-liquid contact angle). Zuber (1957) predicted the CHF would occur when the vapor columns (see Section 1.1.1) become unstable due to a Kelvin-Helmholtz instability. The assumption that this instability is responsible for the transition from nucleate boiling to film boiling allowed him to relate the CHF to fluid properties using Equation 5

$$q''_{CHF} = \frac{\pi}{24}\rho_v^{1/2} h_{fg} \sqrt[4]{\sigma g(\rho_\ell - \rho_v)} \tag{5}$$

where ρ_v and ρ_ℓ are the vapor and liquid densities respectively, h_{fg} is the latent heat of vaporization, σ is the surface tension, and g is the acceleration due to gravity. While Equation 5 was derived for a horizontal infinite plate under saturated conditions, other researchers (Bobrovich, Gogonin et al. 1964; Lienhard and Watanbe 1965; Lienhard 1970) extended his theory for different geometries by relating the CHF for a specific geometry to the Zuber CHF for a horizontal infinite plate by a function of a dimensionless characteristic length, L', shown in Equations 6 and 7. L and $f(L')$ are

geometry specific and were calculated for several different geometries by Lienhard and Dhir (1973b) to be:

$$q''_{CHF} = \frac{\pi}{24} f(L') \rho_v^{1/2} h_{fg} \sqrt[4]{\sigma g(\rho_\ell - \rho_v)}, \tag{6}$$

$$L' = L\sqrt{\frac{g(\rho_\ell - \rho_v)}{\sigma}}. \tag{7}$$

More recently, Kandlikar (2001) developed models to incorporate surface orientation, surface-liquid contact angle, and liquid subcooling into a prediction of the CHF. The correlation accounting for the surface orientation and surface-liquid contact angle (Equation 8), which is valid for flat surfaces with orientations between ϕ = 0° (horizontal) and 90° (vertical), indicates that the CHF decreases as both the contact angle, β, and the surface orientation, ϕ, increase. The model shows good agreement with experimental results from (Lienhard and Dhir 1973a) and many other researchers and is given as:

$$q''_{CHF} = h_{fg} \rho_v^{1/2} \left(\frac{1+\cos\beta}{16} \right) \left[\frac{2}{\pi} + \frac{\pi}{4}(1+\cos\beta)\cos\varphi \right]^{1/2} \left[\sigma g(\rho_\ell - \rho_v) \right]^{1/4}. \tag{8}$$

Kandlikar's model to incorporate liquid subcooling into a prediction of the CHF is

$$q''_{CHF,SUB} = q''_{CHF,SAT}\left(1+\frac{T_{SAT}-T_{SUB}}{T_S-T_{SAT}}\right), \tag{9}$$

where $q''_{CHF,SUB}$ is the CHF under subcooled conditions, $q''_{CHF,SAT}$ is the CHF under saturated conditions, T_S is the surface temperature at the CHF, T_{SUB} is the bulk temperature of the subcooled liquid, and T_{SAT} is the saturation temperature of the liquid. The CHF in a subcooled system is greater than the CHF in a saturated system due to additional heat transfer to the subcooled liquid. Experimental evidence has shown the relationship between CHF and liquid subcooling to be linear for water and several other fluids (Kutateladze and Schneiderman 1953).

Recent work by Nikolayev et al. (2006; 2006) has indicated that the transition to CHF may not be the result of the Kelvin-Helmholtz instability of the vapor columns but of a phenomena known as the vapor recoil mechanism. Vapor recoil is the force on the vapor-liquid interface of a vapor bubble caused by an evaporating molecule leaving the interface. The force is normal to the interface and directed towards the liquid side. On a per unit interface area basis, the vapor recoil force is

$$F_r = \eta^2\left(\frac{1}{\rho_v}-\frac{1}{\rho_\ell}\right) \tag{10}$$

where η is the evaporation rate per unit area and ρ_v and ρ_ℓ are the vapor and liquid densities, respectively. The evaporation rate is largest close to the bubble's contact line with the surface, so the vapor recoil force is strongest in this region. As the heat flux increases, so does the evaporation rate. When the CHF is reached the vapor recoil force is

strong enough to pull the contact line out and collapse the bubble into a vapor film. When the temperature of a system is far from the critical temperature of the fluid, the surface tension and the vapor recoil force are of the same order and a force balance on the interface can be rearranged to give the Zuber prediction (Equation 5). However, when the system temperature is near the critical temperature, surface tension becomes less important than gravity and the vapor recoil mechanism gives a very different prediction of the CHF than the Zuber prediction. Near the critical temperature, the vapor recoil mechanism better predicts experimental observations of the CHF.

Correlations have also been derived to estimate the amount of heat transfer from a boiling surface using both fluid properties and surface geometries. Mikic and Rohsenow (1969) proposed a correlation for boiling heat transfer that included the heat transfer due to transient conduction into the liquid at a bubble boundary and natural convection on inactive areas of the heater. Judd and Hwang (1976) accounted for the evaporation from the microlayer of liquid beneath a vapor bubble (Equation 11) as

$$q'' = 2K\sqrt{\pi\rho_\ell c_\ell k_\ell f_b}R_b^2 N_a \Delta T + (1 - K\pi R_b^2 N_a)\overline{h_{nc}}\left(T_S - T_{SAT}\right) + \rho_\ell h_{fg} N_a f_b \overline{V_{ME}}\,, \qquad (11)$$

where K is a ratio of the surface area influenced by a bubble to the projected area of the bubble on the surface, ρ_ℓ, c_ℓ and k_ℓ are the density, specific heat and thermal conductivity of the liquid respectively, f is the bubble liftoff frequency, R_b is the radius of a bubble at departure, N_a is the nucleation site density, T_S is the surface temperature, T_{SAT} is the saturation temperature, $\overline{h_{nc}}$ is the average natural convection coefficient on inactive areas of the heater, h_{fg} is the latent heat of vaporization, and $\overline{V_{ME}}$ is the volume of the

microlayer. Mikic and Rohsenow found good agreement with experimental results when $K = 4$, while Judd and Hwang found $K = 1.8$ with the addition of the microlayer evaporation. (See also the work of Das et al (2006)).

2.2 Enhanced Boiling

Passive methods for enhancing boiling heat transfer are attractive because no power is required to facilitate the enhancement. Most passive methods involve modifying the boiling surface (reviewed by Webb (1981)) to either increase the number of active nucleation sites or increase the ease with which a bubble forms, grows, and releases from a nucleation site. It has been known since the 1930's that roughening a surface can lead to an increase in the number of nucleation sites, and therefore improve nucleate boiling. Jakob and Fritz (1949) tested a surface roughened by sandblasting and a machine grooved surface (0.016 mm square with 0.48 mm spacing) and reported an increase in the heat transfer as much as three times the heat transfer from a comparable smooth surface. Unfortunately, these improvements could not be repeated after the surface had been submerged for several hours or days. Ostensibly, trapped air or vapor that provides nucleation sites is displaced by liquid (particularly if the surface is cooled below the saturation temperature). Since these early investigations, surfaces with artificial nucleation sites have become commercially available (e.g. Fujikaka's ECR-40 (1980) surface, the Thermal excel-E surface, and the Gewa-T surface). All of these surfaces contain subsurface cavities or grooves to trap additional air or vapor and replenish flooded nucleation sites.

An important parameter that affects the efficiency of boiling heat transfer surfaces is surface wettability. Gaertner (1965) coated a heater with a hydrophobic fluorocarbon film and observed that bubbles quickly covered the entire surface resulting in a very low CHF. Liaw and Dhir (1986) and Maracy and Winterton (1988) demonstrated that the maximum heat flux decreases with a decrease in the surface wettability. Dhir and Liaw (1989) explained the effect of surface wettability on maximum heat flux using the concept of void fraction. The void fraction is the ratio of the non-wetted area of the surface to the total area. For a similar volume of vapor, the void fraction will be higher on a hydrophobic surface than on a hydrophilic surface due to the increased footprint of vapor bubbles on a hydrophobic surface. Thus, less liquid is allowed to contact the surface, resulting in a lower heat flux. Takata et al (2003; 2005) investigated the effects of a superhydrophilic surface of titanium dioxide on pool boiling. This surface has the unique property that its wettability varies with exposure to ultraviolet light, thus the efficiency of the boiling can be controlled. The authors reported that the critical heat flux from the coated surface is about two times as large than that for an uncoated copper surface. However, the problem is that the coating often results in a large thermal resistance (even for very thin coatings). In a recent paper on boiling over a superhydrophobic surface, Takata et al (2006) reported that at contact angles over 150° film boiling occurs at very low wall superheats, and nucleate boiling is barely observed.

Several investigators have tried to use surface wettability to improve the performance of heat transfer surfaces. Young and Hummel (1965) sprayed a stainless steel surface with polytetrafluoroethylene (PTFE or Teflon®) (30–60 0.25 mm spots per cm^2) and observed a dramatic increase in heat transfer, especially at low wall superheats.

The discontinuities in surface wettability allowed a bubble to nucleate easily and quickly grow to the size of the hydrophobic dot, but prevented the bubble from quickly covering the whole surface in vapor. This concept was patented by Hummel (1965). Gaertner (1967) patented a similar design which utilized mechanically created nucleation sites (conical cavities) coated with PTFE to ensure nucleation occurred in the center of a hydrophobic spot. The design resulted in a slight improvement in the heat transfer compared to Hummel's design, though Gaertner still had problems with the nucleation sites flooding when the heat was cycled on and off over a period of days.

Another approach for improving the heat transfer characteristics of a surface is by the use of dissimilar materials. Fujita and Uchida (1998) created a composite surface consisting of copper cylinders imbedded in a stainless steel plate. The surface took advantage of the different thermal conductivities of the two materials to attain a higher temperature on the surfaces of the copper cylinders and thus ensure that nucleation first occurred there. Measurements indicated an approximately 50% improvement in heat transfer as compared to a similar surface made of a single material, though the reason for the improvement is not entirely clear.

Active methods for enhancing boiling heat transfer involve an external power input to facilitate enhanced boiling. Common methods (not including acoustic methods) are flow boiling and jet impingement. Mudawar and Maddox (1989) demonstrated critical heat fluxes as high as 360 W/cm^2 from vertical boiling surfaces containing microchannels or small fins by flowing FC-72 over the surfaces at 4 ml/s. Presumably the flow increases convection and detaches bubbles from the surface due to the resulting drag. Marsh and Mudawar (1989) also investigated a falling liquid film as a means to

enhance boiling heat transfer. The falling film provided similar benefits as a forced flow, but with lower power input requirements due to the assistance of gravity. Numerous investigators, e.g., (Monde and Katto 1978; Ma and Bergles 1983) have used impinging jets to enhance boiling heat transfer from a surface. Tillery et al. (2006) used an impinging synthetic jet to increase the heat transfer from a water-submerged copper surface at 120°C by 282%.

2.3 Bubbles in an Acoustic Field

Numerous investigators have shown that a gas bubble can be forced to oscillate in a variety of different modes and even levitate in the presence of an acoustic field (Leighton 1994). Bubble oscillations can be in the form of volume oscillations, e.g., Trinh et al. (1998) or capillary surface waves, e.g., Koster and Sani (1990). The evolution of capillary waves on the surface of a spherical liquid shell was investigated by Holt and Trinh (1996) who found that the onset of these capillary waves is dependent on a minimum sound pressure amplitude and analogous to the classical Faraday waves (Faraday 1831). Fourier analysis of the capillary waves indicates that the waves have a finite number of discrete frequencies. However, as the shell wall thins or the sound pressure is increased the spectrum becomes broadband and the shell is covered by many chaotic capillary waves.

Gas bubbles in an acoustic field are also subjected to primary and secondary Bjerknes forces that are well understood for spherical gas bubbles (Leighton 1994). Hao et al (2001) numerically studied the effect of the secondary Bjerknes force on vapor bubbles near a plane rigid surface. Their numerical method assumed a potential flow and

hence modeled the effect of the wall as an image bubble of equal size located an equal distance from the opposite side of the rigid plane. The image bubble oscillated in phase with the real bubble; hence the presence of the wall resulted in an attractive force between the bubble and the wall.

2.4 Acoustic Enhancement of the Boiling Process

The effect of ultrasonic sound waves on nucleate pool boiling was investigated by Isakoff (1956). He observed an improvement in the critical heat flux, but no shift in the boiling curve. In later investigations, Ornatskii and Shcherbakov (1959) and Romie and Aronson (1961) determined that the effect of ultrasonic vibrations is to reduce the bubble size and increase the frequency of bubble formation. Wong and Chon (1969) investigated the effect of ultrasonic vibrations on both natural convection and pool boiling using ultrasound (20.6 kHz to 306 kHz), and showed that below a critical sound pressure the effects on heat transfer are negligible. Above this critical sound pressure, they found that, while natural convection is significantly enhanced, there is a negligible effect on nucleate boiling. More recently, Park and Bergles (1988) investigated pool boiling in an ultrasonic cleaning bath (at 55 kHz modulated at 120 Hz) and found that for saturated boiling, the heat flux decreases in the presence of ultrasound, but in subcooled boiling, there is an improvement of 5–10%.

Ho-Young et al (2004) conducted ultrasonic experiments (at 48 kHz, which was also a resonance frequency of their test vessel) that confirmed that heat transfer is enhanced for natural convection, but that enhancement is severely reduced at the onset of boiling. They also found that heat transfer is enhanced more for subcooled boiling compared with saturated boiling, and that the enhancement is higher at low heat flux

boiling than high heat flux boiling. As shown by these authors, the ultrasonic waves produce cavitation bubbles in the liquid that result in improved that which increases the convection coefficient. When boiling begins, the natural motion of the vapor bubbles has the same effect as the cavitation bubbles, therefore diminishing their effects. In saturated boiling little to no cavitation occurs because the gas solubility is so low, so any improvements are due to acoustic streaming. It was observed that, in saturated boiling, the size of the vapor bubbles is reduced when ultrasound is present, possibly due to increased bubble departure frequency. The lower improvement at higher heat fluxes was attributed to the more vigorous movement of vapor bubbles that made the effects of ultrasound less pronounced. A number of other researchers, including Iida and Tsutsui (1992), Wong and Chon (1967), and Markels et al (1960) found that the CHF is increased by the use of ultrasonic vibrations.

Sitter, Snyder, Chung, and Marston (1998a; 1998b) examined boiling on a wire in the presence of a standing acoustic wave in both terrestrial and microgravity experiments. Standing waves driven by piezoelectric actuators (at 10.18 and 27.2 kHz) led to an increase in the heat transfer coefficient for any relative position of the wire in the standing wave, but the increase was most dramatic when the wire was placed at the acoustic pressure antinode forcing the bubbles that had grown larger than resonance size to migrate towards the pressure node.

Hao et al (2001), who numerically investigated the effect of the secondary Bjerknes force on a vapor bubble near a rigid wall, found that when the acoustic wave fronts are parallel to the wall a vapor bubble is held near the wall by the secondary Bjerknes force. However, when the acoustic wave fronts are perpendicular to the wall,

the bubbles moved laterally along the wall due to the primary Bjerknes force. The investigators proposed that the lateral movement of the vapor bubbles could be utilized to improve boiling heat transfer.

Heffington and Glezer (2004) used a technique known as vibration induced bubble ejection (VIBE) in which vapor bubbles are removed from a boiling surface by pressure oscillations produced by a acoustic driver vibrating at ultrasonic frequencies. The pressure oscillations generated instabilities at the vapor/liquid contact lines resulting in the bubbles being ejected from the surface. Preliminary work on this technology indicates that significant improvements in boiling heat transfer (78% for distilled water at a T_S = 120°C) and critical heat flux (425% for a 70/30 mixture of water and methanol) are possible.

CHAPTER 3

EXPERIMENTAL APPARATUS AND PROCEDURES

The removal of vapor bubbles from a flat boiling heat transfer surface by acoustic forces is investigated using a submerged acoustic driver comprised of a piezoelectric diaphragm and a plastic holder. The effects of the acoustic forces are first investigated using air bubbles injected underneath a horizontal surface. Then, vapor bubbles are generated on a heated surface that is designed to produce an isolated vapor bubble of a prescribed size. Global heat transfer improvement is quantified using a copper heater instrumented with embedded thermocouples.

3.1 The Acoustic driver

The submerged acoustic driver (Figure 3) is comprised of a piezoelectrically driven diaphragm mounted in a sealed cylindrical tube. The unimorph diaphragm is comprised of a 19.7 mm piezoelectric disk bonded between a 0.10 mm thick 31.2 mm diameter stainless steel disk and an 18.2 mm diameter electrode. The characteristic resonance frequency and resonance impedance, reported by the manufacturer, are 1.3 ±0.5 kHz and 300 Ω respectively. The thickness of the entire diaphragm is 0.22 mm. The diaphragm is mounted at the end of a 50 mm long 26.6 mm diameter plastic tube such that the electrode faces the inside of the tube. The second end of the cylindrical tube is sealed with a thin brass disk. For underwater operation the inner volume of the tube is vented to the atmosphere through a small diameter flexible tube that also contains the two

driver leads. The acoustic driver is driven by a laboratory function generator and a high-voltage (up to 120 V_{rms}) amplifier. The driving frequency is between 0.1 and 20 kHz.

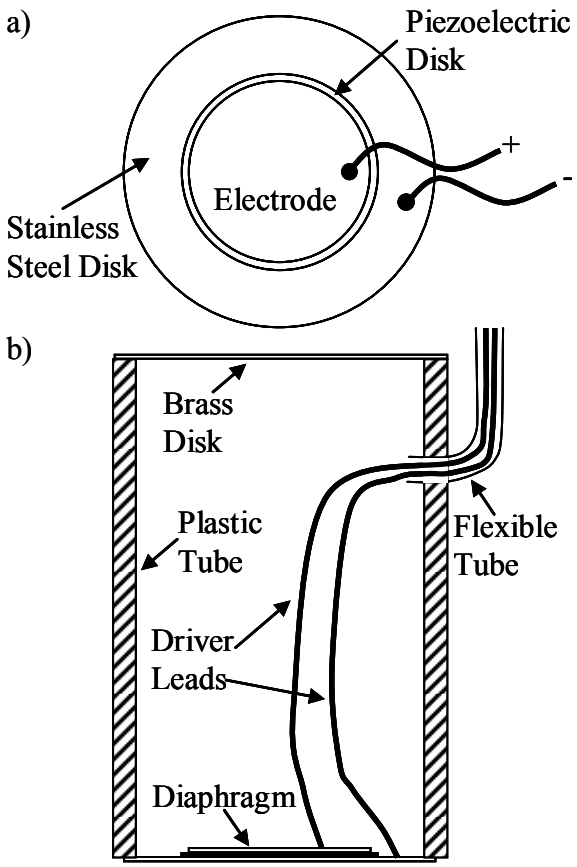

Figure 3. Assembled acoustic driver. a) Top-view of piezoelectric diaphragm, and b) cross-section of entire acoustic driver.

The sound pressure level produced by the submerged acoustic driver is determined using a calibrated hydrophone (Brüel & Kjær Type 8103) placed opposite to and along the centerline of the piezoelectric diaphragm. The peak-to-peak sound pressure over a range of input voltages up to 115 V_{rms}, and frequencies between 0.25 and 20.25 kHz, at separation distances of 1, 2, and 3 centimeters was measured. The

hydrophone voltage was converted to pressure using the manufacturer's calibration tables.

The results from the hydrophone measurements were used to verify a numerical calculation of the sound field. In the numerical solution, the pressure at a given point is determined by considering the differential contribution to the pressure from a differential area of the piezoelectric diaphragm (Leighton 1994). The contribution of each differential area is assumed to be that of a hemispherical source, though the magnitude of the source is quadratically dependent on the differential area's location on the piezoelectric diaphragm. The expression is then integrated over the surface of the diaphragm to arrive at the total gauge pressure at a given point (Equation 12). The pressure field is assumed to be axisymmetric.

$$P(r,z,t) = \int_0^{2\pi}\int_0^R \frac{\Psi_0}{r'}\left(1-\frac{a^2}{R^2}\right)\exp\{i(\omega t - kr')\}a\,da\,d\theta \tag{12}$$

$$r' = \sqrt{(r-a)^2 + a^2\sin^2\theta + z^2} \tag{13}$$

The origin of the *r*- and *z*-coordinates is at the center of the piezoelectric diaphragm. ψ_0 is an empirically determined constant. r' is the distance from the point (*r*,*z*) to the differential area on the piezoelectric diaphragm's surface and is determined by Equation 13. θ and a are dummy variables representing the azimuthal and radial locations of the differential area on the diaphragm's surface. ω and k are the angular driving frequency

and the wave number, respectively. R is the radius of the piezoelectric diaphragm that is free to oscillate and is thus equal to the inside radius of the cylindrical plastic tube.

When the acoustic driver is placed near a rigid wall, the sound field in the region between the driver and the wall is calculated by assuming a total reflection of the sound from the wall. Mathematically, this is achieved by adding a mirror image of the acoustic driver an equal distance, d, on the other side of the plane representing the wall-fluid interface. In this case, the pressure at a point between the real driver and the wall is calculated using Equations 13-15. r'' is the distance between the point (r, z) and the differential area on the image piezoelectric diaphragm's surface.

$$P(r,z,t) = \int_0^{2\pi}\int_0^{R} \frac{\Psi_0}{r'} e^{i\omega t}\left(1-\frac{a^2}{R^2}\right)\left(\frac{e^{-ikr'}}{r'}+\frac{e^{-ikr''}}{r''}\right) a\, da\, d\theta \tag{14}$$

$$r'' = \sqrt{(r-a)^2 + a^2\sin^2\theta + (2d-z)^2} \tag{15}$$

3.2 Air Bubbles Test Apparatus

The effect of acoustic forces on a gas bubble without the added complication of controlling a boiling surface is investigated using an apparatus for forming single, trapped air bubbles. Air bubbles are formed underneath a horizontal submerged surface such that the buoyancy force acts towards the surface. While the dynamics of these bubbles is quite different from that of vapor bubbles on a boiling surface, it allows for assessment of some of the effects of acoustic excitation on gas bubbles in liquids.

The air bubbles test apparatus consists of a 51 x 51 x 6.7 mm aluminum plate suspended under the free surface of a water tank. A one millimeter diameter hole was drilled in the plate, through which a 0.9 mm diameter hypodermic needle was inserted so that its end is flush with the aluminum plate. Air bubbles are formed by injection from a hypodermic syringe. The acoustic driver (Section 3.1) is submerged in the water tank below the plate such that the piezoelectric diaphragm is concentric with the injection needle as shown in Figure 4. The effect of the acoustic field on the suspended air bubble is recorded using a Kodak Motion Analyzer (capable of recording speeds up to 10,000 fps) and Nikon 55 mm lens.

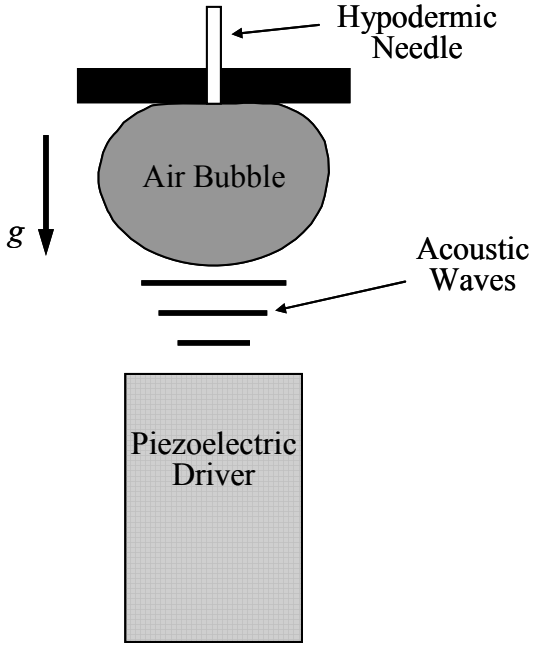

Figure 4. Schematic of air bubbles test apparatus (not shown to scale).

The size of the air bubble is determined by manually controlling the volume of air injected. Buoyancy pushes the bubble against the aluminum plate causing the bubble to be shaped like slightly squashed spheres (Figure 4). Bubble sizes are compared by

measuring the horizontal equatorial diameter. During a test, bubble sizes are estimated using a calibrated scale and the live video feed. Later, during image processing, a more precise measurement of the bubble size is determined from the digitized images. Bubble sizes between two and seven millimeters in diameter are easily attainable using this apparatus.

The digitized images of the captured air bubbles are analyzed using MATLAB software. The diameter of a single bubble in an image is determined by converting the original gray scale to a black and white using an adjustable intensity threshold. In the images, the bubble is darker than the white background, so the value of the intensity threshold is adjusted by trial and error for each image or set of images until the result of converting the original image is a black and white silhouette of the bubble. A MATLAB function is then used to determine the perimeter of this silhouette by finding white pixels which are adjacent to black pixels. This perimeter image is used to determine the diameter at the bubble's equator using the known magnification. This procedure is applied to all images in a video sequence. These data yield the time dependence of the bubble diameter to determine oscillation frequency. In addition, the frequencies of surface oscillations on the bubble are determined by analyzing the reflection of light (from a lamp) from the bubble into the camera. The surface oscillations change the angle of a bubble's surface, and thus change the amount of light that reaches the camera. The time dependence of pixel intensities in a video sequence are used to determine surface oscillation frequencies.

3.3 Single Vapor Bubble Produced on a Heated Surface

Since a single vapor bubble is not easily found on a common boiling surface, a single bubble heater was designed to provide a boiling surface that produces a single vapor bubble of a consistent, controllable size and at a specific location (the buoyancy force is normal to and directed away from the surface).

The surface (see Figure 8) consists of an insulating annulus surrounding a thermally conductive 2.4 mm diameter pin. The top surface is machined smooth and electroplated with a copper coating. The thermally conductive pin provides a thermal path for heat to travel from the heater below to the exposed surface, resulting in a hot spot on the surface. The power can be controlled so that only the hot spot is above the saturation temperature of the fluid, while the rest of the surface remains cooler. Centered in the hot spot is a hydrophobic dot made by applying a thin coating of a fluorourethane to the surface. The dot provides a preferential nucleation site and controls the size of the contact line of the resulting bubble. The design of the single bubble heater was largely influenced by the work of Fujita and Uchida on boiling from composite surfaces (1998) and a patent by Hummel involving boiling on surfaces with heterogeneous contact angles (1965).

In the present design, the core of the single bubble heater is a 38.1 mm diameter copper cylinder heated by a 15.7 mm cartridge heater coated with high thermal conductivity paste inserted into a hole in one end. The single bubble heater core is shown in both exploded and assembled views in Figure 5. The top end of the copper cylinder is abruptly narrowed to a 2.4 mm diameter cylindrical pin. A brass ring is soldered to the copper cylinder so that the top surface of the ring is even with the flat surface created by

the abrupt change in diameter of the copper cylinder. A stainless steel annulus with an inner diameter equal to the diameter of the small copper pin is placed around the pin and bolted to the brass ring. The top surface was electroplated with copper and machined smooth such that the boundary between the stainless steel plate and the copper pin is indistinguishable. A picture of the electroplated top surface is shown in Figure 6.

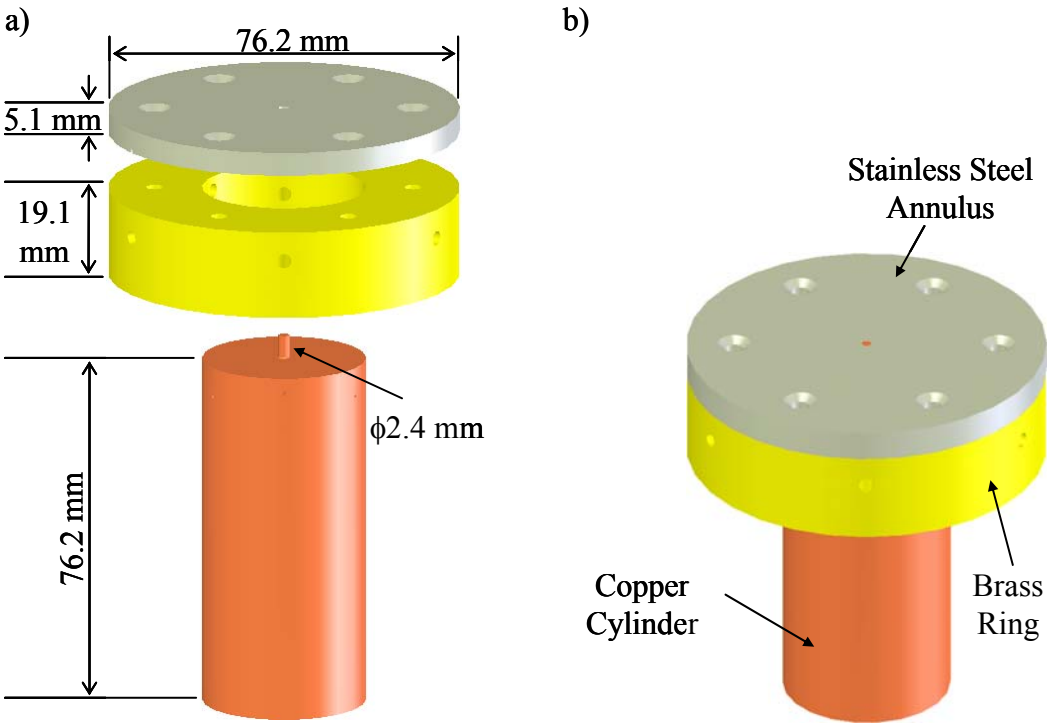

Figure 5. a) Exploded view of single bubble heater core, b) assembled view.

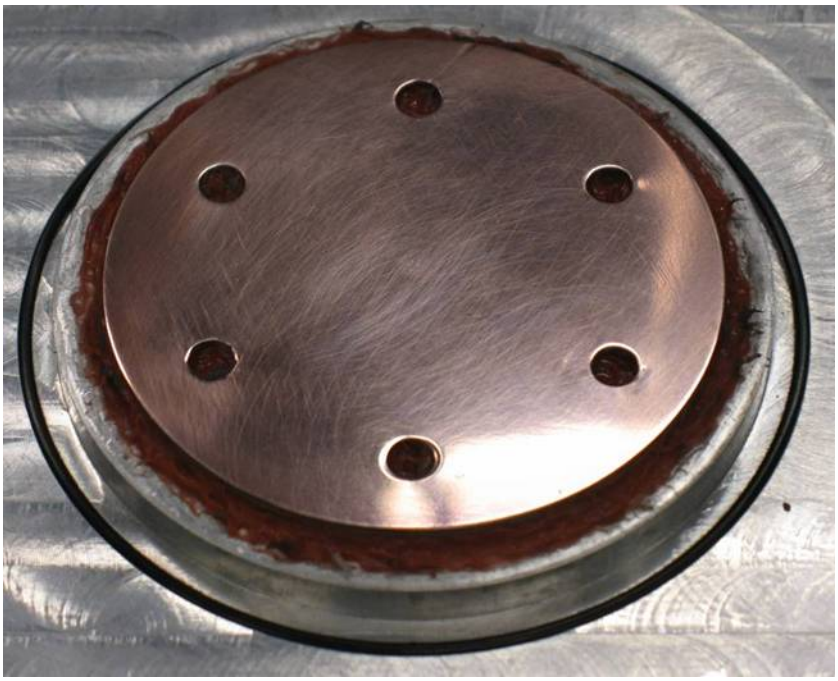

Figure 6. Picture of electroplated top surface of single bubble heater.

The heater core is placed in a housing assembly (Figure 7) that creates a fluid chamber and seals all but the top surface of the heater core from the boiling fluid while allowing optical access to the boiling surface. The housing assembly consists of a 100 mm pipe sandwiched between two aluminum plates. A phenolic disk thermally insulates the bottom of the heater core from the lower aluminum plate. The heater core is sealed to the upper aluminum plate. A glass cylinder is glued to a mounting ring and bolted to the upper plate to form the fluid chamber above the heater. The glass cylinder can be easily removed to allow easy access to the top surface of the heater core.

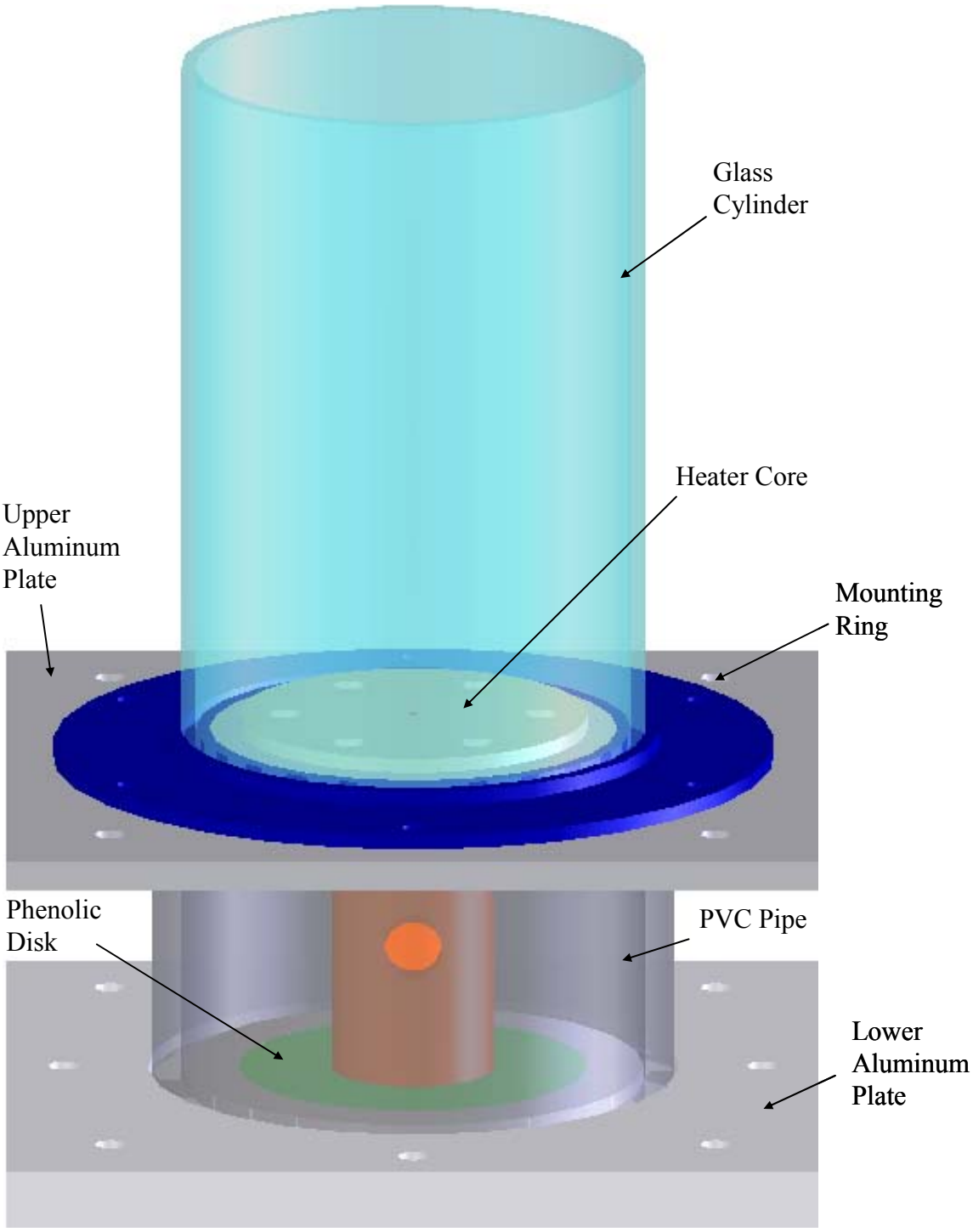

Figure 7. Housing assembly for single bubble heater.

The thermal conductivity of the copper cylinder and pin is 385 W/m^2K while the thermal conductivity of the 304 stainless steel is only 18 W/m^2K. Therefore heat is conducted through the copper pin to the heater's surface with much less resistance than through the stainless steel annulus. The result is a hot spot in the center of the surface directly above the copper pin.

After careful cleaning of the heater's surface a small 1.6 mm diameter hydrophobic dot (FluoroPel PFC 502 IBA fluorourethane) was applied at the center of the hot spot using a capillary tube. The hydrophobic dot was air dried, and then cured by heating the surface to 120°. After curing, deionized water had a contact angle with the hydrophobic dot of 116°. Note that the cleaned electroplated copper surface has a contact angle of 30°. The hydrophobic dot provides a preferential nucleation site and the edge of the dot determines the contact line of the resulting bubble. A close up schematic of the copper pin, stainless steel annulus, electroplated surface, and hydrophobic dot is shown in Figure 8.

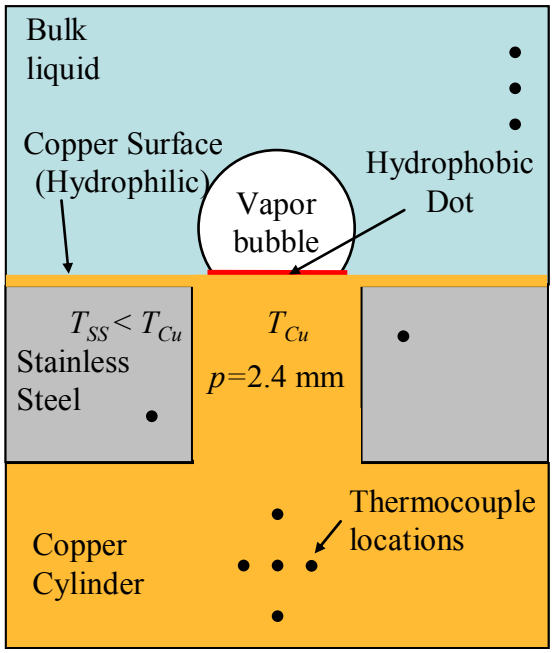

Figure 8. Close-up schematic of copper pin, stainless steel annulus, electroplated surface and hydrophobic dot (not to scale).

Six thermocouple sensors are placed within the copper cylinder and brass ring of the heater core (Figure 8). Three are located at the centerline of the copper cylinder 3.2 mm, 6.4 mm, and 9.6 mm below the flat surface created by the abrupt change in diameter at the base of the copper pin. The other three thermocouples are 6.4 mm from the centerline of the copper cylinder and are located 6.4 mm below the flat surface. These three holes are evenly distributed at 120° degree intervals around the circumference of the cylinder. Two more thermocouples are placed in the stainless steel annulus. These are 5.1 mm from the centerline and are located 1.3 mm and 2.6 mm below the heater's surface. Finally, three thermocouples are inserted through the sides of the glass cylinder at distances of 31.8 mm, 57.2 mm, and 82.6 mm above the heater's surface. The thermocouple outputs are read using a standard laboratory data acquisition system. The centerline thermocouple located 9.6 mm below the abrupt change in diameter is used as

an input to a temperature controller for the cartridge heater. The voltage and current to the cartridge heater are monitored to determine the power dissipation and are recorded by the data acquisition system.

Before conducting an experiment, the acoustic driver (Section 3.1) is suspended in the fluid chamber at a set distance above the surface. In most cases the piezoelectric diaphragm is parallel to the surface. The cartridge heater is turned on and the set point on the temperature controller is slowly increased until nucleation occurs in the center of the exposed surface, directly above the copper pin. Care is taken not to increase the temperature past the point at which at which nucleation occurred away from the center of the exposed surface and the hydrophobic dot. The on-off action of the temperature controller is sufficient to maintain the temperature at the location of the input thermocouple within a one degree window (±0.5°C) of the set point. Once a vapor bubble is formed and grows to cover the hydrophobic dot, the acoustic driver is used to induce acoustic forces and excite bubble instabilities. These effects are captured using the Kodak Motion Analyzer. The camera is angled down at 15° below the horizontal to avoid refraction effects caused by the thermal gradient.

3.4 Calibrated Copper Heater

Heat transfer measurements are performed using a calibrated copper heater that is the same heater used by Tillery (2004; Tillery, Heffington et al. 2006) with a few minor modifications. Tillery's heater was based on similar heaters created by Sellers (2000) and Sheffield (1994). The following description closely follows the descriptions by Tillery.

The calibrated copper heater core (Figure 9) consists of a copper cylinder 54 mm long and 22.2 mm in diameter. One end of cylinder is tapered to a diameter of 14.1 mm and then squared so that the cross-section is a 10 mm x 10 mm square. A 9.5 mm diameter cartridge heater is inserted into the circular cross-section end of the core. Two thermocouples are inserted into the square cross-section at each of three locations (3.2 mm, 6.4 mm, and 9.6 mm below the surface).

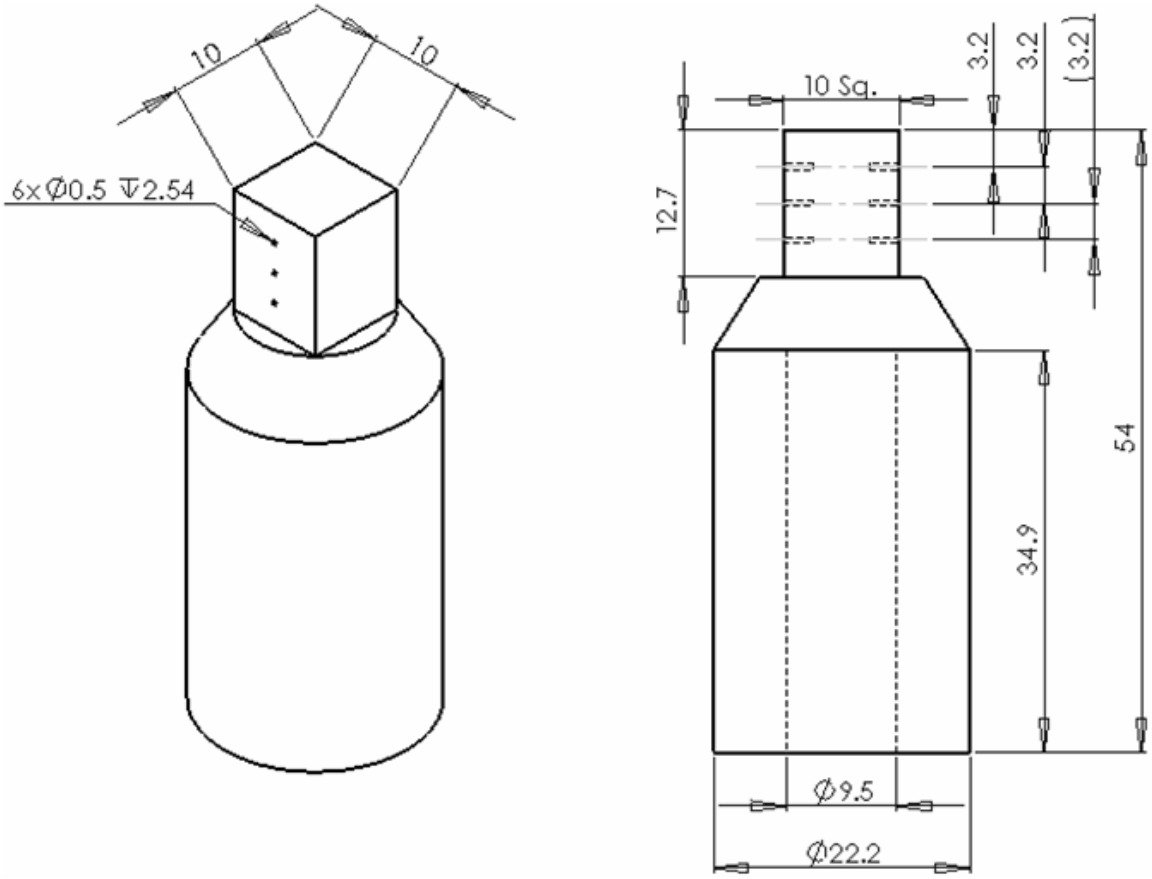

Figure 9. Drawing of calibrated copper heater core (all dimensions in millimeters).

The calibrated copper heater core is sandwiched between two fiberglass plates (Figure 10). The top fiberglass plate has a 10 mm x 10 mm square hole in its center to expose the top surface of the heater core. The space between the calibrated copper heater

core and the walls of the enclosure is insulated with packed fiberglass insulation to maximize heat transfer through the exposed surface. In addition to all the components shown, a 127 mm diameter clear acrylic cylinder is attached to the upper fiberglass plate to form a fluid chamber.

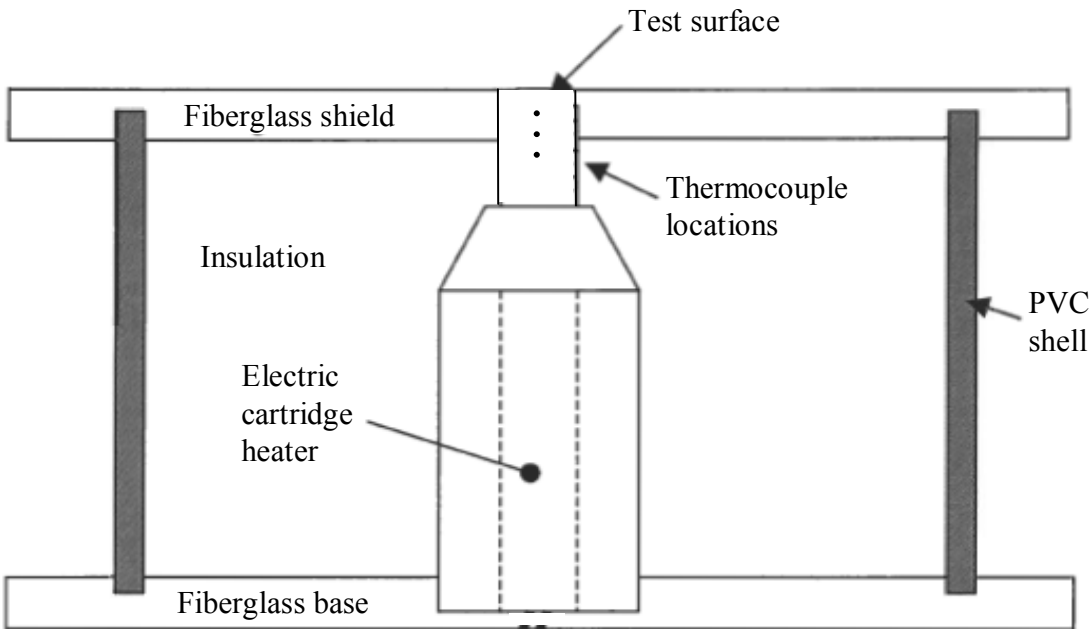

Figure 10. Cross-section of calibrated copper heater.

The cartridge heater is powered by a standard laboratory variac (0–240V) and the thermocouples are read using a laboratory data acquisition system. Temperature readings are taken at a frequency of 1 Hz. The readings from the six thermocouples are used to extrapolate the surface temperature and surface heat flux. By varying the voltage supplied to the cartridge heater the surface heat flux can be controlled.

The surface heat flux and surface temperature of the calibrated copper heater are extrapolated from thermocouple readings at points below the exposed surface using

Fourier's law and the assumption that the heat flux is one dimensional in the top section of the calibrated copper heater core. The constant cross-section of the top section and insulation of the side surfaces are the basis for this assumption. The thermal conductivity of the copper is 390 W/mK and the cross sectional area is 1 cm^2. For all calculations involving the calibrated copper heater, the temperature at a particular thermocouple level is considered to be the average of the readings from the two thermocouples at that level. All heat flux calculations are performed using the temperature difference between the thermocouples closest to the exposed surface and those farthest from the exposed surface. Surface temperature is extrapolated from the temperature readings of the thermocouples assuming a linear temperature profile.

Before using the calibrated copper heater, the exposed surface of the core is sanded with 600 grit sandpaper to remove any oxidation from the copper. Then, the surface is polished. After polishing, the surface is cleaned with soap and water, then ethanol, then acetone, and finally rinsed with deionized water. At this point, the fluid chamber is filled with deaerated, deionized water. The cartridge heater is turned on and the voltage supplied slowly increased until nucleate boiling occurs on the surface. The boiling is allowed to continue, with care taken to keep the heat flux below critical heat flux, for one hour. Allowing the water to boil on the surface is an effective method for better cleaning the surface to ensure that the maximum critical heat flux is attained both with and without acoustic enhancement.

After preparing the heater's surface, the fluid chamber is drained and the acoustic driver suspended in the chamber at the desired distance from the surface, and the fluid chamber is filled with fresh deaerated, deionized water. The acoustic driver is turned on

and set to the desired voltage and frequency. The heat flux through the surface is increased by increasing the voltage supplied to the cartridge heater until the critical heat flux is reached. At this point, the cartridge heater is quickly turned off to prevent damage to the calibrated copper heater by the rapid increase in temperature that occurs at the critical heat flux. Temperature data throughout the experiment are recorded and used to calculate the surface temperature and surface heat flux, while the Kodak Motion Analyzer is used to visually record the experiment. For each position of the acoustic driver this process is repeated several times both with and without the acoustic driver activated in order to establish the critical heat flux and boiling curve both with and without the effect of the acoustic enhancement.

CHAPTER 4

CHARACTERIZATION OF THE ACOUSTIC DRIVER

The sound pressure amplitude (P_a) produced by the acoustic driver is measured as a function of driving frequency (f_D), driving voltage (V_D), and axial distance from the surface of the piezoelectric diaphragm (z). Due to the size of the hydrophone, all measurements are performed in a nine liter water tank instead of the fluid chambers in the single bubble (Section 3.3) or calibrated copper (Section 3.4) heaters. Reflections from the walls are assumed to be negligible due to the thinness of the tank walls and their distance (>150 mm) from the acoustic driver. The experimental results were used to verify a numerical solution of the pressure field, and are measured using the procedure outlined in Section 3.1.

Figure 11 shows the sound pressure dependence on driving frequency at an axial distance of 1 cm and a driving voltage of 35 V_{rms}. The sound pressure is low below 750 Hz and is almost frequency invariant above 1.25 kHz.

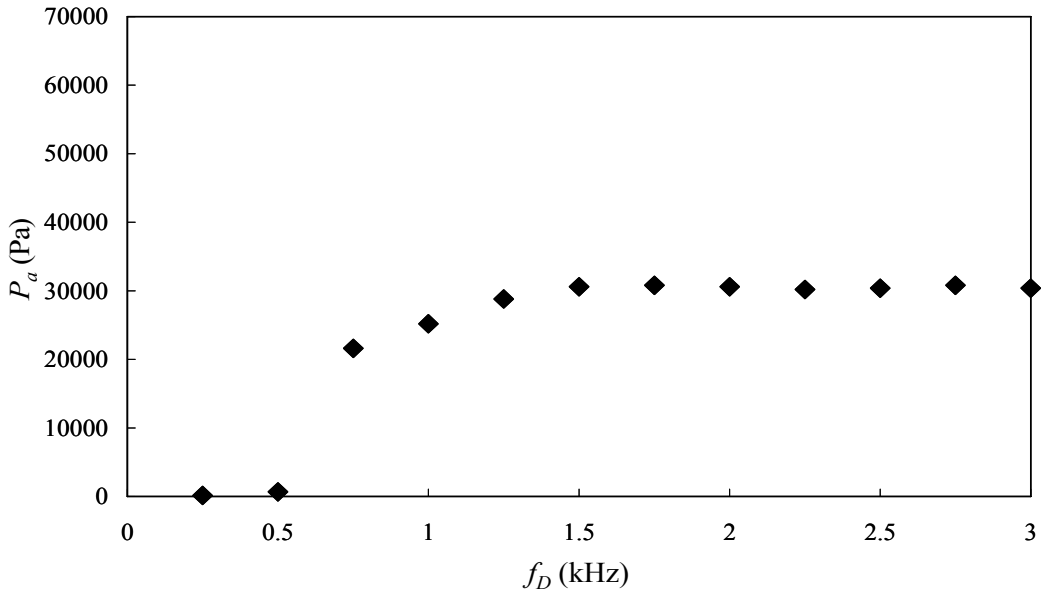

Figure 11. The variation of the sound pressure with driving frequency (z = 1 cm and V_D = 35 V_{rms}).

The sound pressure amplitude is also directly related to the driving voltage. Figure 12 illustrates how the sound pressure increases with driving voltage (f_D = 1 kHz, z = 1 cm). At driving voltages above 75 V_{rms} the performance of the acoustic driver degrades owing to strain and the driver eventually fails.

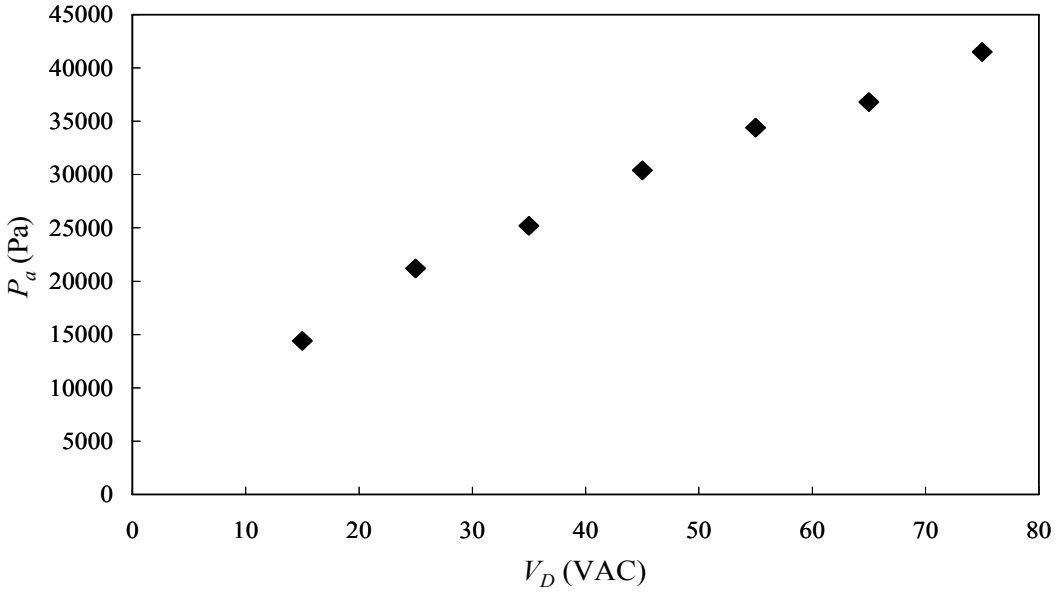

Figure 12. Variation of the sound pressure with driving voltage (z = 1 cm and f_D = 1 kHz).

The sound pressure amplitude decreases rapidly with axial distance due to spreading and attenuation of the sound waves as shown in Figure 13 at axial distances of 1, 2, and 3 cm.

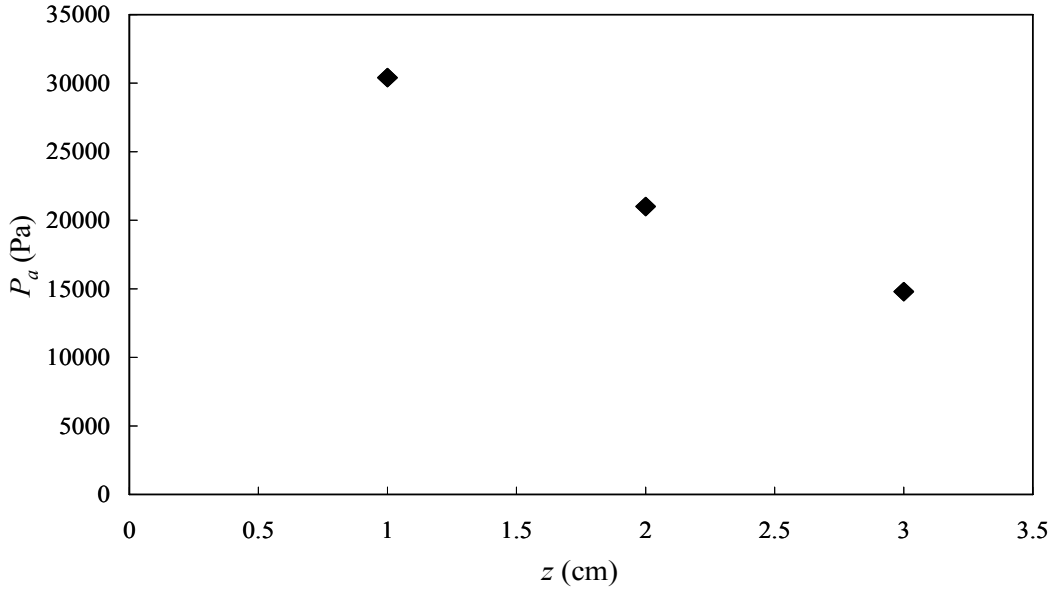

Figure 13. Graph showing the sound pressure amplitude's dependence on axial distance from the piezoelectric diaphragm (f_D = 3 kHz and V_D = 35 V_{rms}).

Equations 12 and 13 in Section 3.1 are used to numerically determine the pressure field as a function of the radial (r) and axial (z) distances from the center of the piezoelectric diaphragm. The variation of the calculated pressure field at 75 V_{rms} and 1 kHz is shown in Figure 14 where the horizontal axis has a maximum value of 2R (twice the radius of the piezoelectric diaphragm). The numerical calculations are in good agreement with the measured pressures (Figure 15) when one pressure measurement is used to empirically determine Ψ_0.

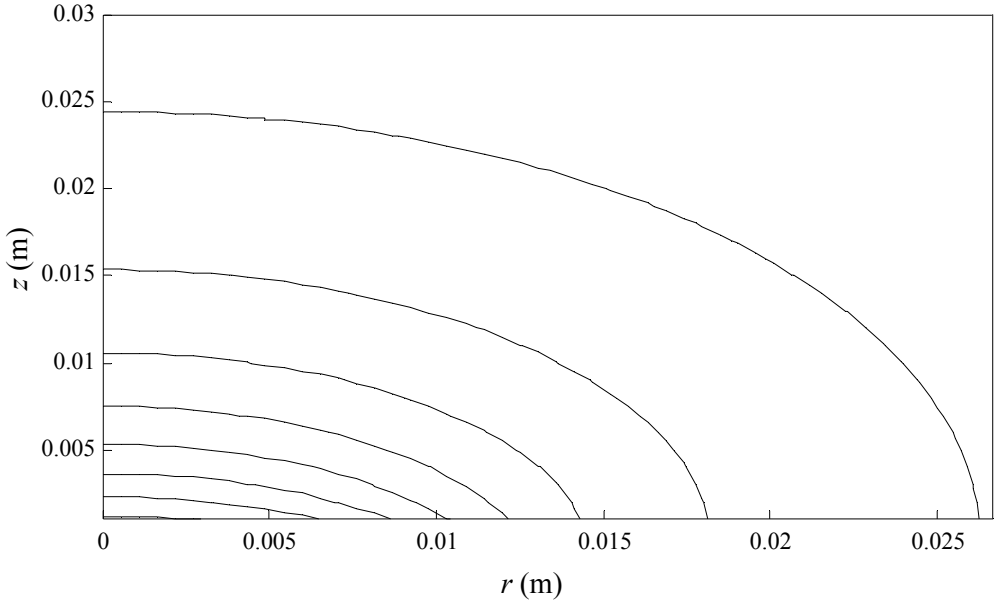

Figure 14. Contour plot of the computed pressure field for f_D = 1 kHz and V_D = 75 V_{rms}. Contour lines decrease from 80 kPa in the lower-left to 20 kPa in the upper-right in 10 kPa increments. (The diaphragm extends from r = 0 to r = 0.0156).

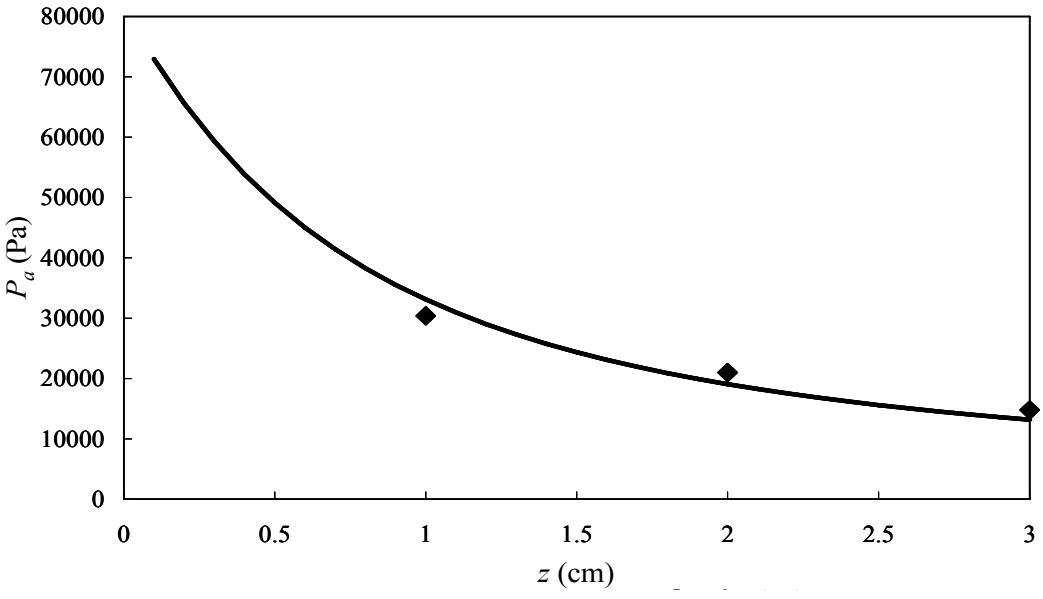

Figure 15. Comparison of numerical (—) and experimental (♦) results for the pressure field at f_D = 3 kHz and V_D = 35 V_{rms}.

When used to excite bubbles in the present work, the acoustic driver is placed in relatively close proximity (~1 cm) to a rigid wall, so the effect of acoustic reflections are not negligible as in the sound pressure measurements described above. The pressure field with a reflection from a nearby parallel rigid wall is estimated using Equations 13-15 (Section 3.1). This pressure field is shown in Figure 16 when the wall is located one centimeter from the piezoelectric diaphragm. In Figure 16, the vertical axis represents the axial distance from the center of the piezoelectric diaphragm, thus the rigid wall is located at the top of the plot. Notice that, near the rigid wall, the pressure gradient has a significant horizontal component.

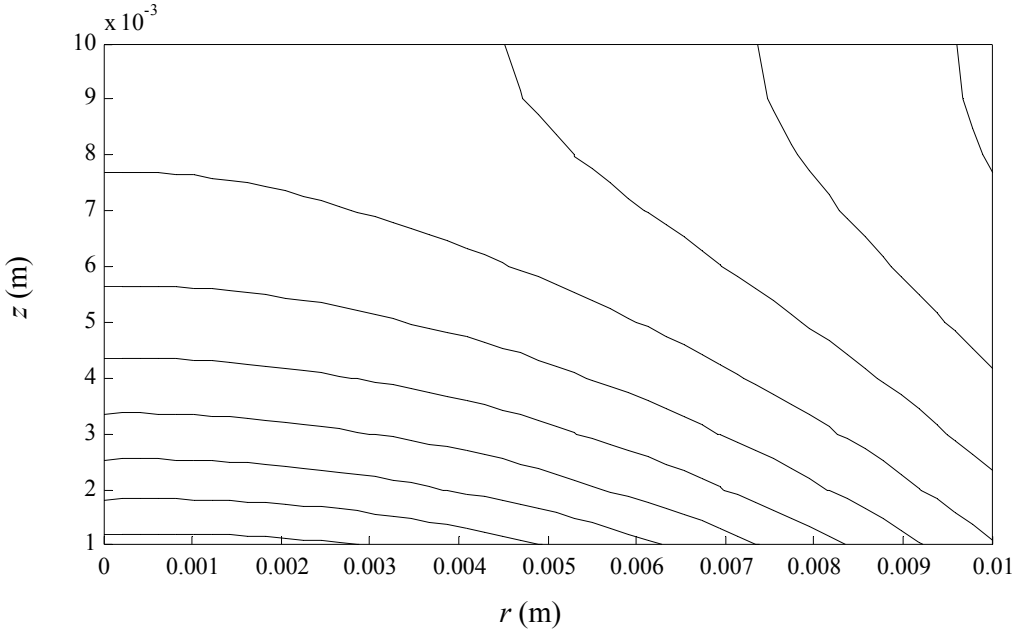

Figure 16. Contour plot of the computed pressure field near a rigid wall normal to the centerline and 1 cm away from the piezoelectric diaphragm. Contour labels decrease from 115 kPa in the lower-left to 70 kPa in the upper-right in 5 kPa increments (f_D = 1 kHz and V_D = 75 V_{rms}).

CHAPTER 5

THE ACOUSTIC EFFECT ON A SINGLE BUBBLE

The results described in this chapter consist of those experiments performed in conjunction with the air bubbles apparatus and the single bubble heater. In these experiments the purpose is to determine the effect of the sound field produced by the acoustic driver on a single bubble. In each case efforts are made to isolate a single bubble of a desired size for study.

5.1 Isolated Air Bubbles

The air bubbles are used to determine the effect of the acoustic field without the added complexity of boiling. In the inverted orientation (Figure 4), the bubble is held against the solid surface by the buoyancy force so it can be studied more easily. In this section the general effects of the acoustic field are described and then the magnitude and frequency of the induced oscillations are quantified.

5.1.1 Bubble Response to an Acoustic Field

A sufficiently high level acoustic field (P_a > 0.5 kPa) induces capillary waves on the surface of the bubble. The frequency to which the bubble responds depends on the characteristic size of the bubble. For a given frequency to which the bubble is receptive, as the sound pressure increases (P_a > 40 kPa), the capillary waves increase in magnitude until the bubble's surface appears to be completely covered by turbulent waves. The violent oscillations of the surface are large enough to break the contact line and detach

the bubble from the surface, even with the buoyant force directed towards the surface. Figure 17 is a series of frames from a video showing the appearance of violent surface waves and the detachment of the bubble (D = 3.2 mm) from the surface after the acoustic driver is energized. The acoustic frequency and sound pressure (computed on the surface at the bubble's centerline) are 2 kHz and 58 kPa respectively.

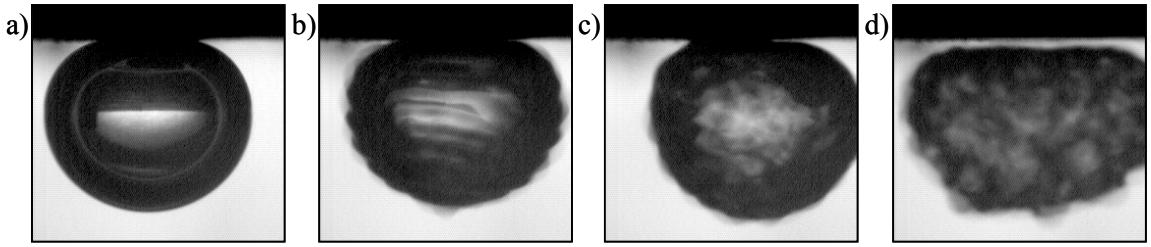

Figure 17. Individual video frames showing the detachment of an air bubble. Times are given relative to the time the acoustic driver was energized. t / T_c = 0 (a), 0.4 (b), 1.1 (c), 3.7 (d).

In Figure 17, time is normalized by a characteristic time, T_c, equal to the circumference of the bubble divided by the propagation speed of the capillary waves. The propagation speed (λf) of the capillary waves can be calculated from Equation 4 in Section 1.1.2. This result is given as

$$\lambda f = \sqrt[3]{\frac{2\pi f \sigma}{\rho_\ell}}. \tag{16}$$

Dividing the circumference of the bubble by the propagation speed gives the characteristic time, T_c, given in as

$$T_c = \frac{\pi D}{\lambda f} = \sqrt[3]{\frac{\pi^2 \rho_\ell D^3}{2 f \sigma}} \,. \tag{17}$$

For the data in Figure 17, the characteristic time is T_c = 10 ms.

Figure 18 is a 2x2 matrix of images showing the effects of different frequencies on bubbles of different size driven at 58 kPa. The bubbles on the left and right columns have diameters, D = 4.1 mm and 5.1 mm, respectively. The bubbles in the upper part of the figure are driven at f_D = 1.5 kHz, while those in the lower part are driven at f_D = 1.1 kHz. Note that the amplitude of the capillary waves is significantly lower when the driving frequency decreases. For the bubble in the right column, the lower driving frequency (1.1 kHz) results in stronger capillary waves than at the higher frequency (1.5 kHz). The relationship between the driving frequency and the bubble diameter is discussed further in Section 5.2.2.

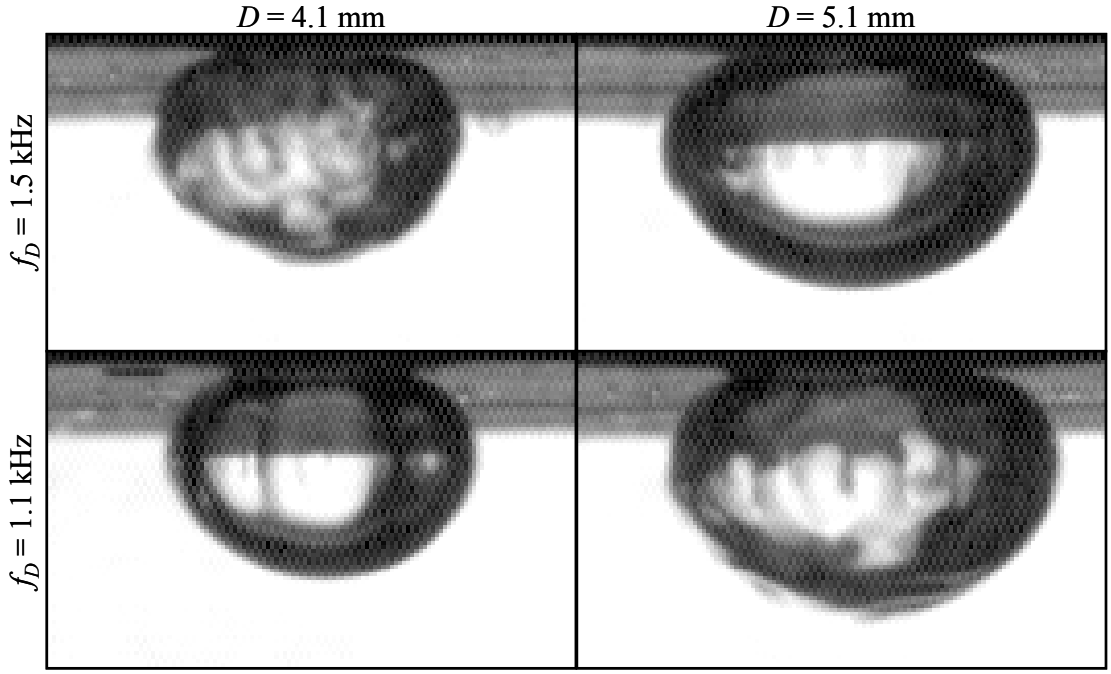

Figure 18. The effect of driving frequency and bubble size on the amplitude of the surface waves.

Experiments are also performed to determine the sound pressure and driving frequency ranges that affect a bubble of a given size. The sound pressure level is held at a fixed level while the driving frequency is varied to determine the minimum and maximum frequencies that result in the appearance of surface waves on the bubble. The presence of surface waves is visually detected. This procedure is repeated at different sound pressure levels. It is found that that as the sound pressure increases, the frequency band in which surface waves are induced on a given size bubble also increases. The surface wave amplitude reaches a maximum at the center of the frequency band. Figure 19 shows an example of this broadening of the frequency band for a 5.9 mm diameter bubble.

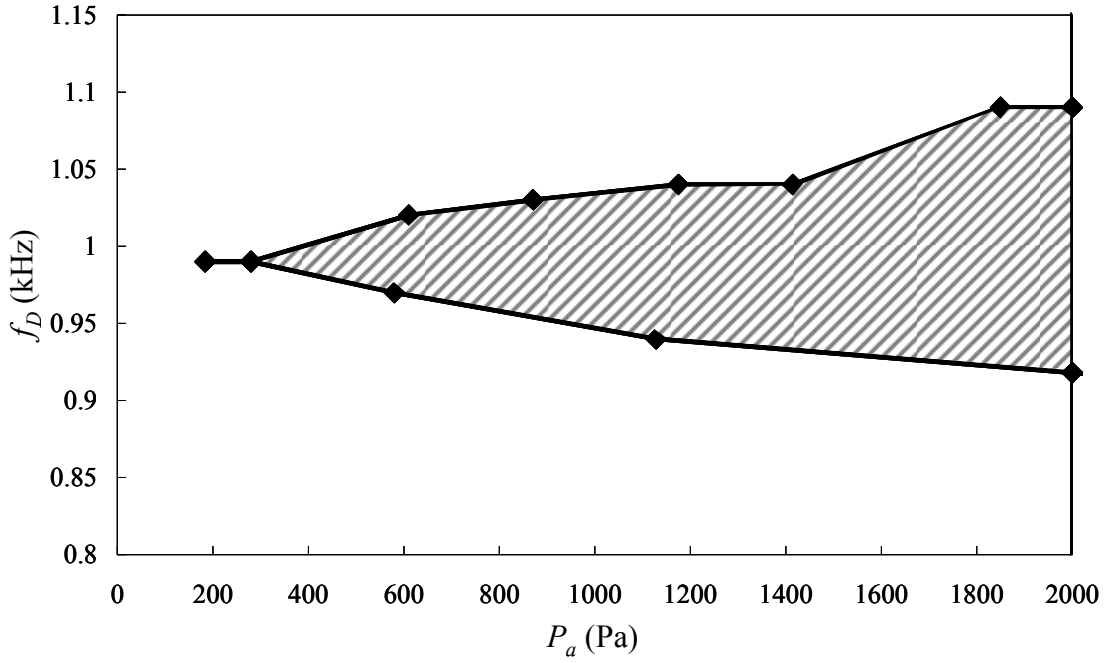

Figure 19. Broadening of the receptive frequency band with sound pressure amplitude for a 5.9 mm bubble.

5.1.2 Contact Line Dynamics

As mentioned in Section 5.1.1, for a given frequency within the receptive band the surface waves increase in magnitude with an increase in the sound pressure amplitude. It is found that, if the amplitude of the waves is sufficiently high, the bubble can detach from the surface. The effect on the contact line of the bubble is captured using high-speed (5000 fps) video. Figure 20 shows a quarter section (allowing for better resolution of the contact line) of a 3.5 mm bubble. The acoustic field has a frequency of 1.3 kHz and the sound pressure amplitude at the centerline of the bubble's base (the upper-right hand corner of each image), as calculated in Chapter 4, is 48.1 kPa. The characteristic time is T_c = 13 ms at 21°C.

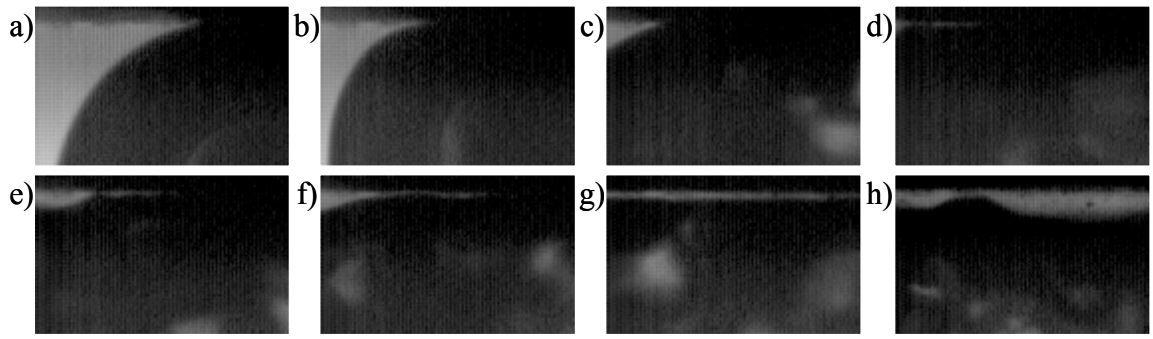

Figure 20. Frames from a 5000 fps video showing breaking of the contact line and detachment of a bubble. D = 3.5 mm, f_D = 1.3 kHz, P_a = 48.1 kPa. t / T_c = 0 (a), 0.4 (b), 0.7 (c), 0.8 (d), 0.9 (e), 1.0 (f), 1.2 (g), 2.8 (h).

The initial acoustic waves ($0 < t / T_c < 0.7$) appear to press the bubble against the surface as seen in frames b and c in Figure 20. During this initial time, the surface of the bubble is smooth and there is no evidence of capillary waves. The bubble is pressed very close to the surface, though it is not clear whether the radius of the contact line is changed. In frame d, capillary waves begin to appear on the bubble's surface and propagate towards the contact line. The motion of the interface appears to push a thin layer of liquid against the contact line, slowly separating it from the surface. The separation of the contact line is first visible as a faint gray line in the upper-left of the frame d. From this point the contact line is quickly contracted and the bubble is "peeled" off the surface. In frame g, the bubble is completely separated from the surface by a 40 μm layer of liquid. The thickness of the liquid layer increases to about 100 μm as shown in frame h. At this point, the separation from the wall is sufficient to allow surface waves to travel along the wall-side surface of the bubble. One of these waves can be clearly seen in frame h. The bubble hovers on this thin liquid layer until either a horizontal force pushes it off the side of the surface or the acoustic driver is turned off.

5.1.3 Frequency Analysis

In addition to the surface waves on the bubbles, the acoustic field also appears to induce radial oscillations in the air bubbles. It is necessary to know how the volume of a bubble changes with time in order to calculate the magnitude of the Bjerknes forces, so successive video frames are analyzed digitally as described in Section 3.2 to obtain a bubble's horizontal equatorial diameter time dependence. The presence of capillary waves on the bubble's surface make it difficult to distinguish between pure radial oscillations and changes in the measured diameter due to the capillary waves. Fourier analysis of the time dependence of the diameter indicates that the diameter oscillates at the frequency of the acoustic field. Figure 21 shows a sample of bubble oscillations. The bubble's equilibrium diameter is 4.41 mm and the average amplitude of the oscillations is about 0.11 mm or about 2.5%. The frequency of the acoustic field is 900 Hz and the pressure amplitude is 41 kPa. While the data in Figure 21 can only be used to calculate a rough estimate of the time dependent volume, due to the added complexity of the capillary waves, it is useful in order of magnitude calculations of the Bjerknes forces.

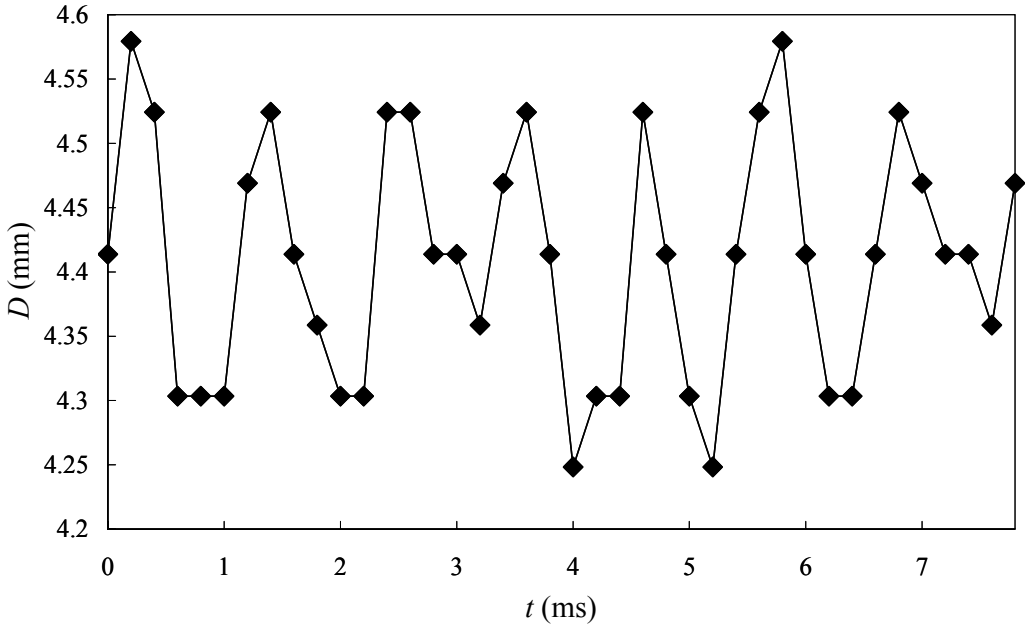

Figure 21. Radial oscillations of an air bubble in a 900 Hz, 41 kPa acoustic field.

Fourier analysis is also used to determine the frequencies of the surface waves using the total reflected light method described in Section 3.2. In this method the sum of all pixel intensities in an image is calculated. Because the surface waves on a bubble change the direction in which light is reflected, the surface waves affect the total amount of light that reaches the camera. The background is assumed to be constant. Fourier analysis is applied to a time series of summed intensity values from a video, taken at 5000 frames per second, to determine which frequencies are present. Figure 22 shows the power spectrum for a 4.25 mm diameter bubble oscillating in a 1.35 kHz acoustic field. The sound pressure at the center of the bubble's base is 14.1 kPa.

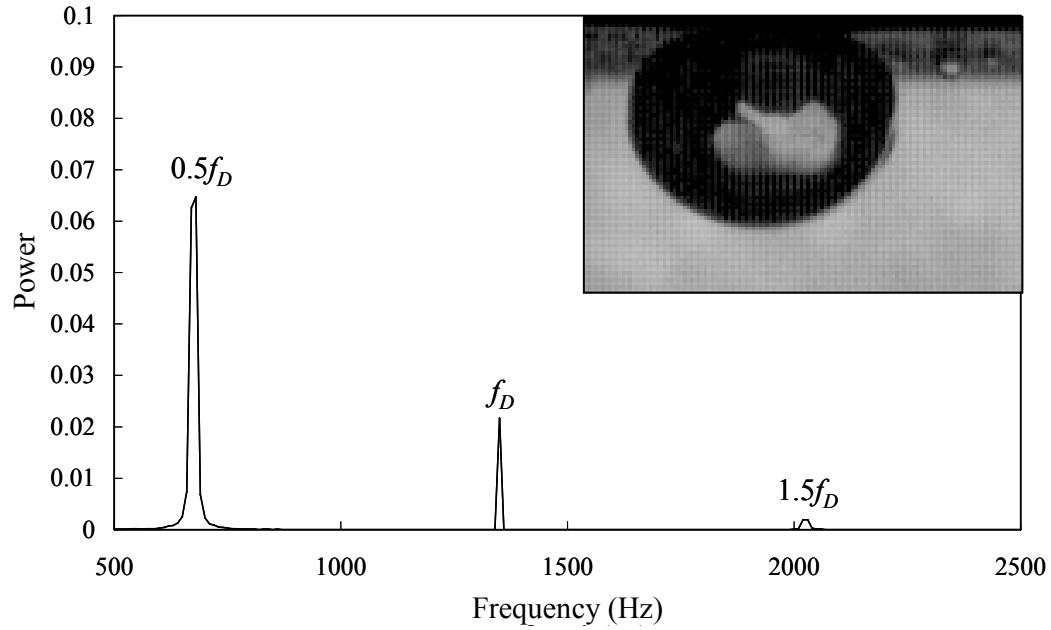

Figure 22. Frequency spectrum of a 4.25 mm diameter bubble in a f_D = 1.35 kHz, 14.1 kPa acoustic field. Top right shows the actual bubble.

Peaks are visible at the driving frequency (f_D), $f_D/2$, and $3f_D/2$. The peak at $f_D/2$ and the hexagonal structure of the bubble's surface lead to the conclusion that Faraday waves (which occur at one-half the driving frequency of the system and often exhibit diamond or hexagonal surface patterns (Holt and Trinh 1996)) may be present in the system.

Figure 23 shows the same bubble as Figure 22 with the sound pressure amplitude increased to 34.3 kPa at the center of the bubble's base. The increase in the sound pressure amplitude results in increased violence of the surface waves. Meanwhile the power in the driving frequency increases and the other peaks begin to broaden. Increasing the sound pressure further (Figure 24 shows P_a = 41.0 kPa) results in full surface turbulence. By this point the driving frequency is dominant and the rest of the spectrum has become broadband.

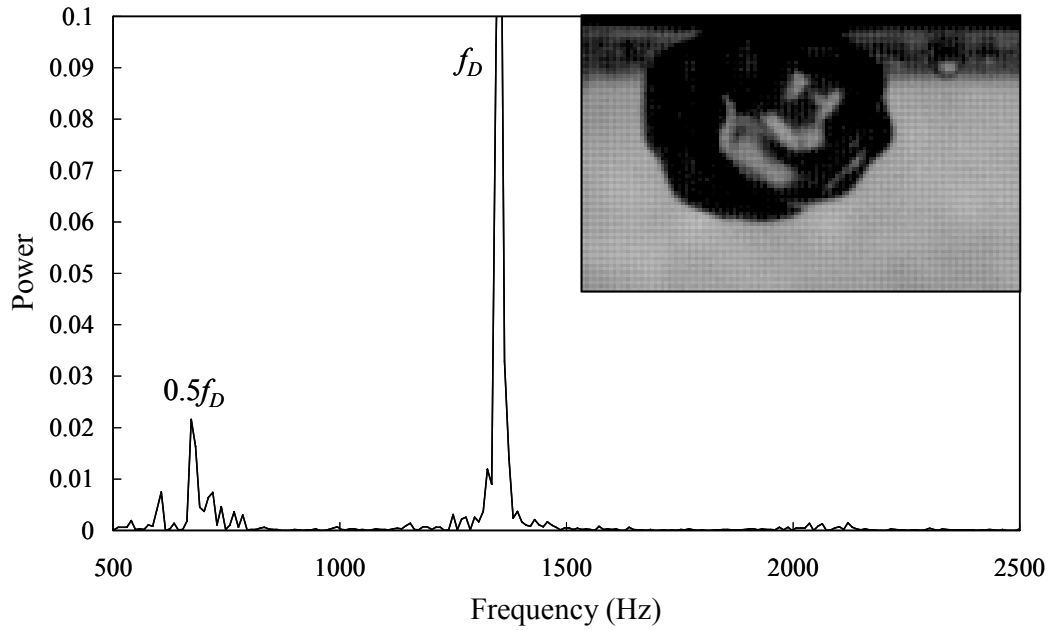

Figure 23. Frequency spectrum of a 4.25 mm diameter bubble in a f_D = 1.35 kHz, 34.3 kPa acoustic field. Top right shows the actual bubble.

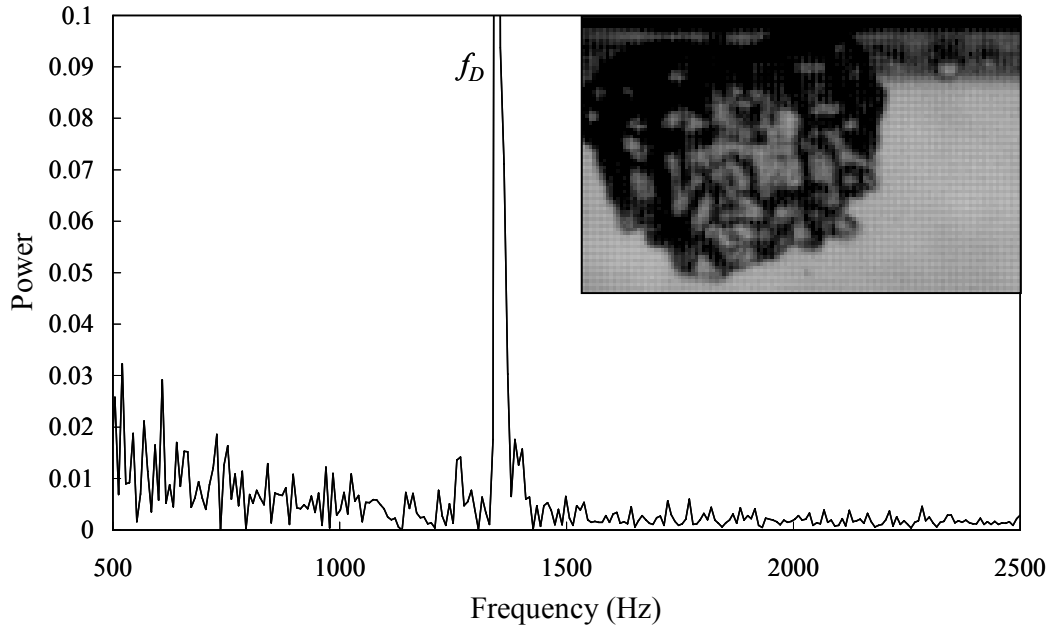

Figure 24. Frequency spectrum of a 4.25 mm diameter bubble in a f_D = 1.35 kHz, 41.0 kPa acoustic field. Top right shows the actual bubble.

5.2 Acoustic Effects on Discrete Vapor Bubbles

5.2.1 Natural Vapor Bubble Formation

Before studying the effects of the acoustic field on a vapor bubble, the natural boiling process on the single bubble heater is characterized. Figure 25 shows the evolution of a natural vapor bubble following its inception to briefly before lift-off. After inception, the bubble grows to cover the hydrophobic dot within 1-2 seconds. As a result of the large contact angle of the hydrophobic dot and the desire of the bubble to achieve minimum surface energy the vapor bubble has a spherical cap shape that sits low on the surface. This is shown in Figure 25a. As the volume of the bubble increases, the contact line remains pinned to the edge of the hydrophobic dot, while the shape of the bubble changes to accommodate the increased volume of vapor. Eventually the bubble takes on a "hot-air balloon" shape like in Figure 25d, where the top of the bubble has a diameter larger than the diameter of the hydrophobic dot and a smaller neck closer to the surface. As the bubble continues to grow the neck is pinched in two, and the top part of the bubble is carried into the bulk fluid by buoyancy, while another spherical cap shaped bubble is left on the surface. The process repeats every 1-3 minutes.

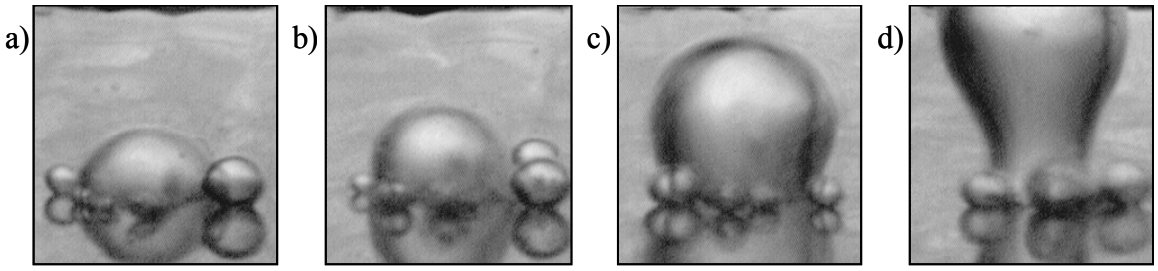

Figure 25. Natural growth of a vapor bubble on the single bubble heater

5.2.2 Effect of an Acoustic Field on a Single Vapor Bubble

An important question is whether capillary waves can also be induced on the surface of vapor bubbles and whether these waves can lead to a breakup of the contact line and detach the bubble from the surface despite the presence of the hydrophobic dot. Figure 26 shows that the capillary waves can indeed be induced on the surface of the vapor bubble. Figure 26a shows a 2.2 mm diameter bubble without the presence of an acoustic field. Figure 26b shows that when the acoustic field is applied (P_a = 56 kPa), surface waves are induced on the surface. As expected, the contact line remains pinned to the edge of the hydrophobic dot. In general, it is observed that the same hydrophobic dot that helps control the size and location of the bubble also hinders its detachment from the surface.

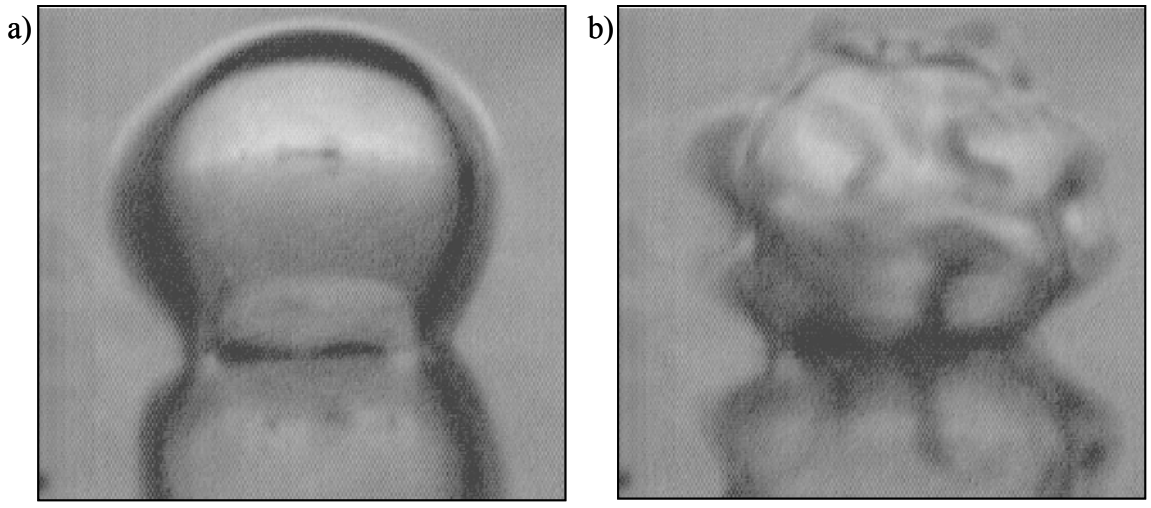

Figure 26. Surface waves induced on the surface of a vapor bubble in a 56 kPa acoustic field. D = 2.2 mm. a) without an acoustic field, b) with the acoustic field.

When the sound pressure amplitude is increased to 86 kPa and the driving frequency of the acoustic field is adjusted to increase the magnitude of the surface waves,

the bubble is detached from the surface. This is shown in a series of high speed video frames in Figure 27. Here the diameter of the bubble is reduced to 1.5 mm and the frequency of the acoustic field is 2 kHz (the characteristic time, T_c, is 5 ms). As for the air bubble in Figure 20, the acoustic forcing first presses the vapor bubble against the surface (Figure 20b). Then, the contact line is then broken (Figure 20c) and the bubble detaches from the surface (Figure 20d). In Figure 20e, the main bubble has left the field of view leaving only smaller bubbles behind.

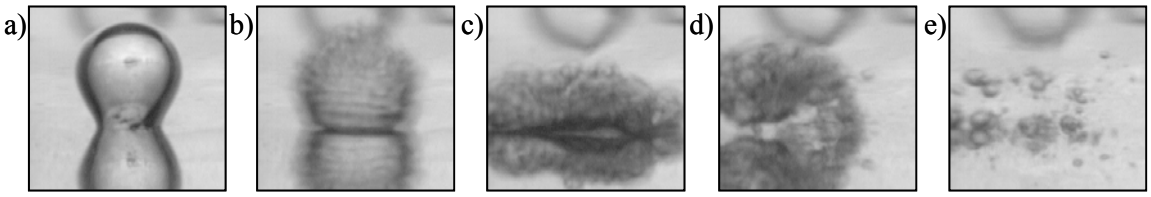

Figure 27. Images showing the complete detachment and near destruction of a vapor bubble. $t / T_c = 0$ (a), 0.4 (b), 1.2 (c), 2.7 (d), 6.2 (e).

As described in Section 5.1.1, capillary waves are induced on the surface of a given air bubble within a certain band of frequencies. As the sound pressure amplitude increases, this range broadens and the amplitude of the capillary waves increases. The amplitude is at its maximum when the frequency is tuned to the center of this frequency band. Experiments with injected vapor bubbles show similarities. One of the goals of the present investigation is to determine the optimal frequency for the removal of a bubble of a given diameter. It is expected that the optimal frequency depends on the diameter, the liquid density, and the surface tension. Dimensional analysis of these parameters produces the dimensionless group α shown in Equation 18. Experimental

observations of the parameters that result in bubble removal indicate that α is approximately constant and equal to 6.7.

$$\left(\frac{D^3 f^2 \rho_\ell}{\sigma}\right) = \alpha \approx 6.7 \tag{18}$$

The optimal frequency for bubble removal (given by Equation 18) is plotted in Figure 28 and shows good agreement with the measurements. Comparison of Equation 18 with the capillary wave equation (Equation 4) indicates that the optimal frequency occurs when the capillary wavelength is slightly more than one-fourth of the bubble's diameter.

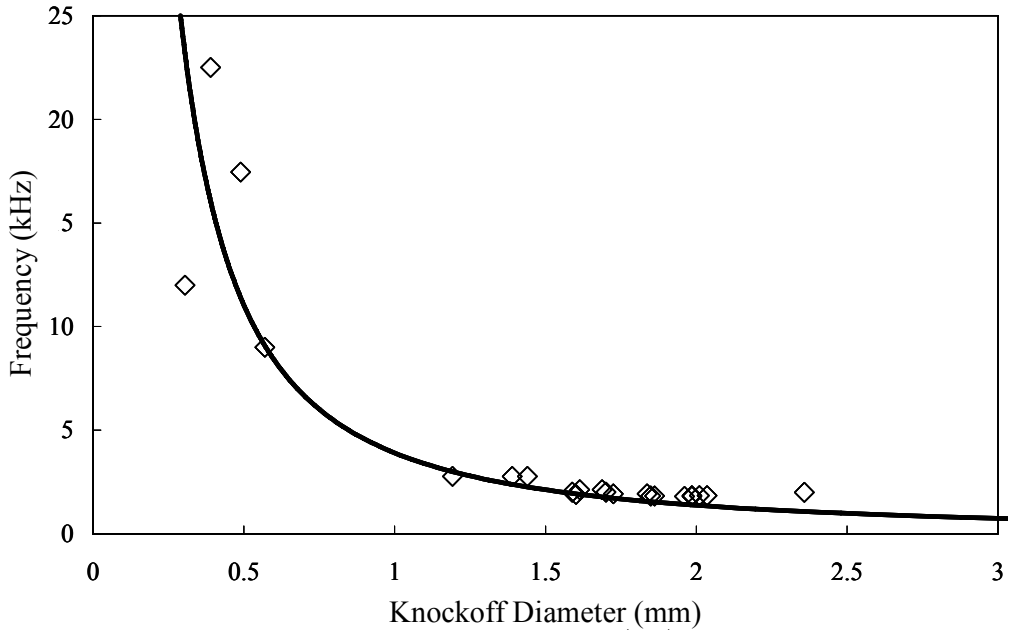

Figure 28. Experimental observations (◊) and prediction (—) of knockoff diameter.

5.2.3 Forces on a Bubble in an Acoustic Field

Figure 29 shows a 1.8 mm diameter bubble that is detached from the heater's surface. However, it appears that the buoyancy force does not immediately advect the bubble from the surface into the bulk liquid. Instead the bubble hovers on a thin layer of liquid, similar to the air bubble in Section 5.1.1. The bubble appears to meander near the surface in the vicinity of the hot spot. The images in Figure 29 show this seemingly random horizontal motion. These images were captured over a time period of approximately 500 ms, but the bubble continued in this pattern for several seconds until the acoustic driver was turned off.

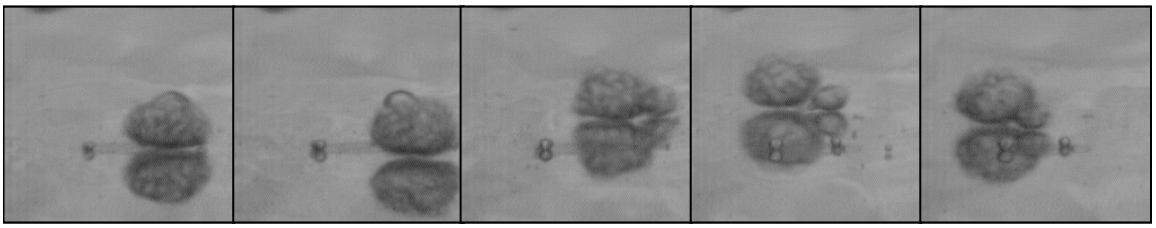

Figure 29. Detached bubble moving in a horizontal plane. (The reflection of the bubble off the surface is clearly visible below the actual bubble).

An experiment is performed where a 3 kHz acoustic signal, sinusoidally modulated at 30 Hz, is used to detach a bubble from the surface (Figure 30a) in order to determine the consequence of removing (and then reapplying) the acoustic signal on a detached bubble. The bubble hovers on a thin liquid layer during the period of the modulation cycle when the acoustic signal is strong enough to induce capillary waves on the surface of the bubble. When the acoustic signal decreases in strength, the surface waves disappear and the bubble begins to rise away from the surface (Figure 30b and c). When the acoustic signal increases in strength once again the surface waves reappear and

the bubble moves back towards the surface (Figure 30e and f). This "bouncing" continued with every modulation cycle.

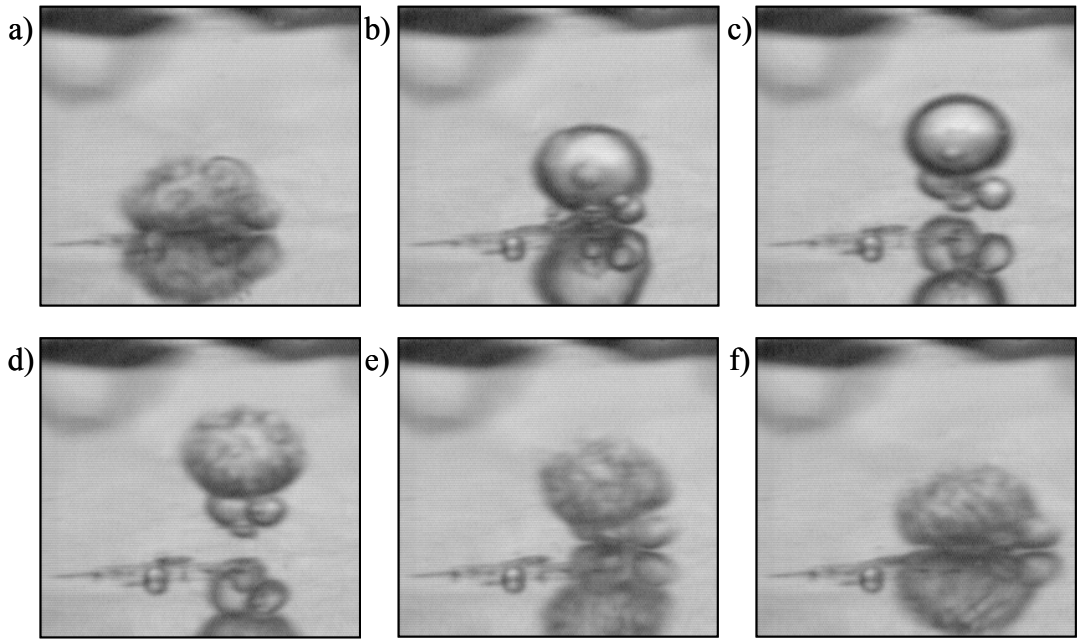

Figure 30. Series of frames showing a bouncing bubble in a 3.0 kHz acoustic field modulated at 30 Hz. $t / T_c = 0$ (a), 1.1 (b), 2.3 (c), 2.7 (d), 3.6 (e), 4 (f). Times are shown relative to frame a. $T_c = 7$ ms.

The force pushing the bubble towards the surface is attributed to the Bjerknes forces (Section 1.1.2). The fact that the attractive force between the bubble and the surface disappears when the acoustic signal decreases in strength indicates that the attractive force must be related to the acoustic signal. Experiments were performed in which a dye was injected into the fluid in the area between the acoustic driver and the wall and no bulk fluid movement was observed. In other experiments, it was observed that bubbles whose sizes fall outside of the range affected by the frequency of the acoustic field were not affected by this force. Therefore, the force is not a drag force

associated with acoustic streaming or some other bulk fluid movement, such as a synthetic jet.

The primary Bjerknes force is actually directed away from the wall in the direction of increasing pressure (see Figure 16) because the bubble is driven below its resonance frequency. However, due the effects of the nearby rigid wall the secondary Bjerknes force is directed towards the wall as discussed in Section 1.1.2. Since, in the presence of the acoustic signal, the bubble is forced towards the surface, the secondary Bjerknes force must be greater than the sum of the primary Bjerknes force and the buoyant force. Frame-by-frame analysis of the video represented in Figure 30 indicates that the bubble takes 2.5 times as long to rise from the surface as it does to be pushed back towards the surface. The approximate acceleration of the bubble is calculated from the video and along with Newton's second law of motion used to estimate that the net force towards the surface when the acoustic field is strong is approximately 6 times the magnitude of the buoyant force.

Estimates of the average buoyant force, F_B, the primary Bjerknes force, F_{B1}, and the secondary Bjerknes force, F_{B2}, are given below for the bubble shown in Figure 30:

$$F_B = \frac{4}{3}\pi R_0^3 \rho_\ell g \approx 7.68\times10^{-5}\ \text{N} \tag{19}$$

$$F_{B1} = -\langle V\nabla P\rangle = \frac{1}{2}V_a \nabla P_a \approx 2.72\times10^{-4}\ \text{N} \tag{20}$$

$$F_{B2} = \frac{2\pi\rho_\ell \omega^2 R_0^4}{r_{12}^2}(\delta R)^2 \approx 8.16\times10^{-4}\ \text{N} \tag{21}$$

The bubble is assumed to be spherical and to have 2.5% radial oscillations (Section 5.1.3). Equations 19-21 show that the secondary Bjerknes force is greater than the sum of the primary Bjerknes force and the buoyant force. The net force towards the surface when the acoustic field is strong is approximately 467 μN or 6.1 times the magnitude of the buoyant force.

CHAPTER 6

CALIBRATED COPPER HEATER RESULTS

The ultimate goal of the present research is to improve the performance of a boiling heat transfer surface. Performance improvements are quantified using the calibrated copper heater (Section 3.4) with and without acoustic enhancement.

6.1 Natural Boiling on the Calibrated Copper Heater

The boiling characteristics in the absence of the acoustic field are characterized with the inactive acoustic driver placed above the heater's surface (Figure 32a). The procedure for using the copper heater is described in Section 3.4.

As boiling begins (Figure 31a), small, approximately spherical bubbles, begin to nucleate on the surface and quickly lift off. The residence time of these bubbles on the surface is nominally less than 1 ms, which is smaller than the characteristic time that is needed to detach a bubble from the surface using the acoustic field (Section 5.1.1). In this short time, a capillary wave does not have time to propagate around the bubble to the contact line to enhance bubble removal before the bubble naturally leaves the surface. As the heat flux increases, the size of the bubbles also increases and these larger bubbles begin to merge vertically with bubbles that are released earlier from the same nucleation sites to form vapor columns (Figure 31b). As the size and number of these vapor columns increases, the columns merge laterally a short distance above the surface to form a larger "molar shaped" bubble with multiple roots extending towards the surface (Figure 31c,d). Finally, when the critical heat flux (CHF) is reached at 333 W/cm^2 (T_S -

T_{SAT} = 40.1°C), this large bubble quickly collapses into a vapor film on the surface (Figure 31e) and the surface temperature increases dramatically. In this experiment, the bulk temperature of the water at the time when the CHF is reached is 80.2°C, representing a subcooling of 19.8°C. Figure 31 shows the natural boiling curve of the calibrated copper heater and representative images at different points on the curve.

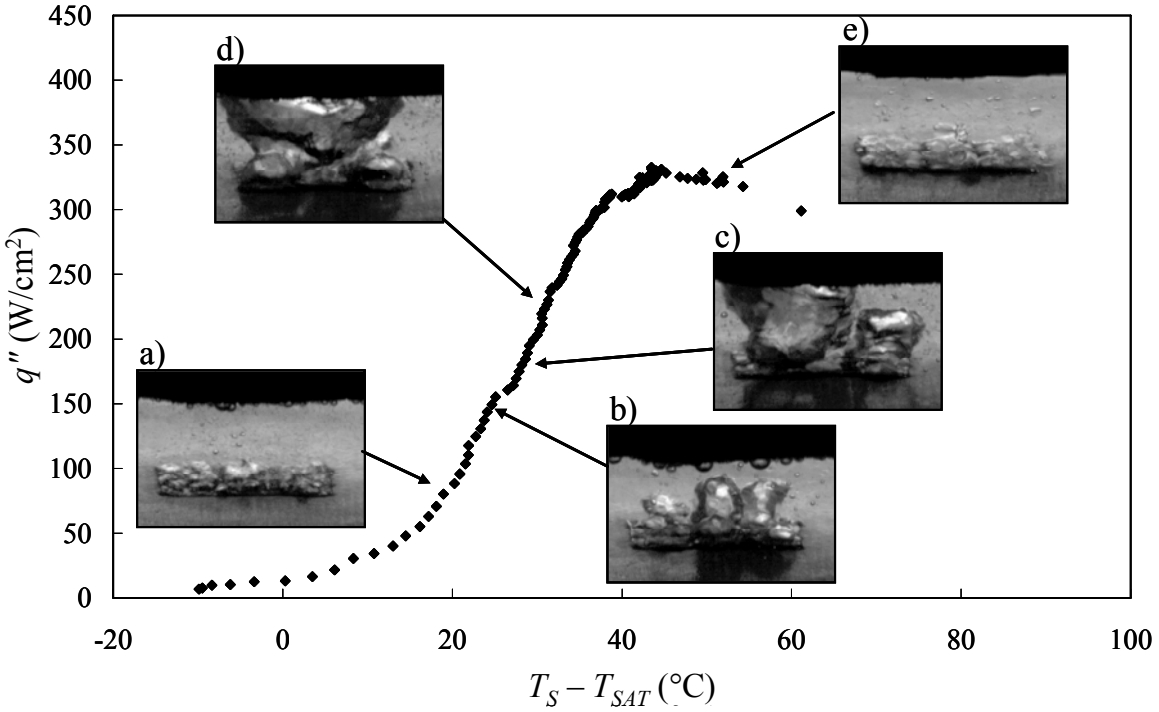

Figure 31. Natural boiling curve of the calibrated copper heater and representative images

6.2 Acoustic Actuation

The experiments described in Section 6.1 are repeated in the presence of acoustic excitation. At low heat fluxes, no difference in the boiling process is observed and small vapor bubbles nucleating on the boiling surface quickly lift off as in the absence of

actuation. As the heat flux is increased, the acoustic enhancement limits the formation of larger vapor bubbles and the vapor columns formed by the merging of these larger bubbles. Figure 32a is an image of the boiling heater surface at a point on the boiling curve (Figure 31) immediately before the CHF in the absence of the acoustic forces. The surface superheat ($T_S - T_{SAT}$) is 44°C and the heat flux is 332 W/cm^2. Figure 32b shows the same surface at the same point on the boiling curve, but with the acoustic enhancement (note that the black object at the top of the images is the acoustic driver).

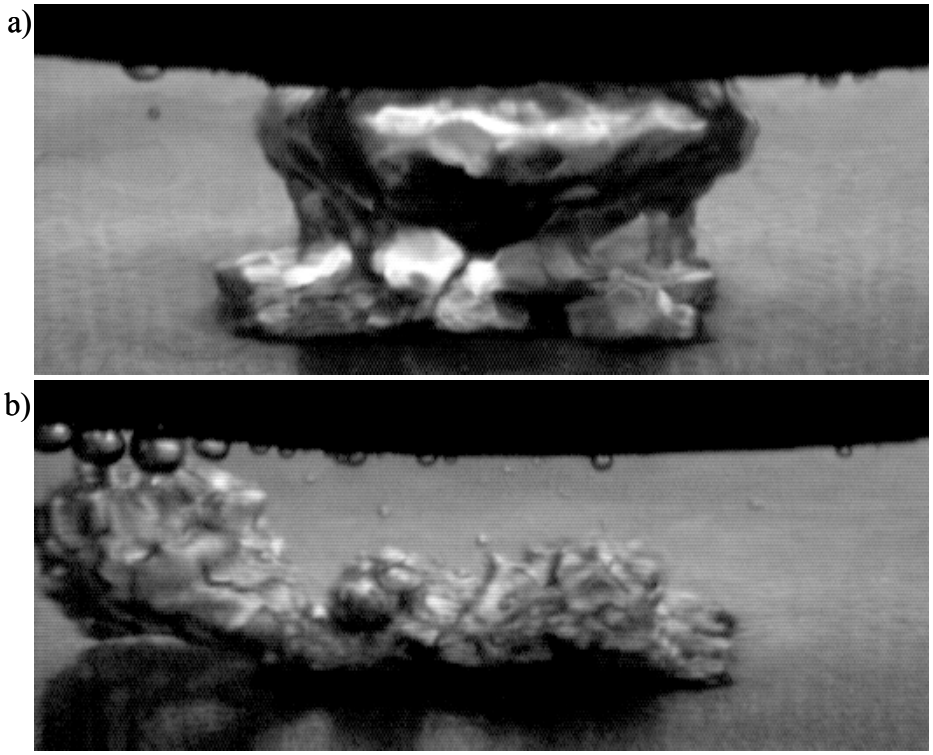

Figure 32. Boiling surface of the calibrated copper heater at T_S - T_{SAT} = 44°C and q'' = 332 W/cm^2. a) No acoustic field, and b) 1 kHz, 70.5 kPa acoustic field at the center of the heated surface.

While the presence of the acoustic field appears to inhibit the formation of large vapor columns, the heat transfer at a given surface superheat is not increased. However,

the actuation increases the CHF and delays transition to film boiling. Figure 33 is a comparison of the boiling curves with and without the acoustic enhancement. The curves coincide until the heat flux exceeds 315 W/cm^2, a point very near the CHF of the surface without actuation. The heat flux with actuation continues to increase until a higher CHF of 404 W/cm^2 ($T_S - T_{SAT} = 49.7$°C), or about a 21% increase, is reached.

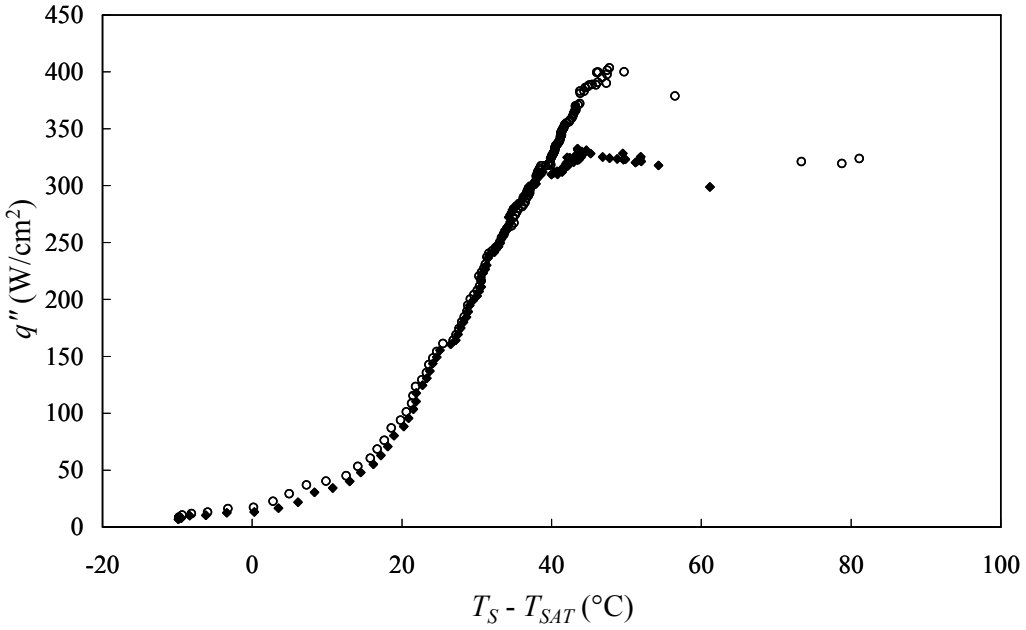

Figure 33. Boiling curves of the calibrated copper heater both with (○) and without (♦) the presence of an acoustic field.

When the acoustic frequency is above 1.2 kHz, no improvements in the critical heat flux are observed. In these experiments the system is brought to near steady state at a certain point on the boiling curve and the frequency of the acoustic field is varied. If the point on the boiling curve is below the unactuated CHF, then for frequencies above 1.2 kHz or below 700 Hz, the boiling surface resembles Figure 32a, which is actually a

picture of the boiling surface with no acoustic actuation. Since the pressure amplitude of the present acoustic driver decreases rapidly below 750 Hz (Figure 11), it is not possible to effectively actuate at low frequencies, and therefore, the present experiments cannot characterize their effect on boiling.

When the acoustic frequency is set to 1 kHz and the system is brought to near steady state above the unactuated CHF, increasing the frequency of the acoustic field above approximately 1.2 kHz (or turning the acoustic driver completely off) results in a rapid collapse to film boiling and a dramatic increase in the surface temperature. Once film boiling occurs, nucleate boiling cannot be reestablished by returning the driver frequency to its effective value. The exact reason why frequencies above 1.2 kHz do not have the same effect on the system as frequencies within the effective range is not completely understood, but it is suspected that the sizes of the vapor bubbles and columns are larger than the size of the bubbles affected by the higher frequencies as discussed in Sections 5.2. The optimal frequency for knocking a single bubble from the surface is given by Equation 18 ($\alpha \approx 6.7$). Thus, for 1.2 kHz an "optimal" bubble size is approximately 2.2 mm. The size of the vapor structures in Figure 32a is approximately 8 mm. Preliminary experiments, using a smaller 2.5 mm square heater, which produces smaller vapor structures, indicate that higher frequencies may be more effective on smaller scale processes.

6.3 Effect of Driver Separation Distance on Critical Heat Flux

For most of the experiments in this work the distance between the heated surface and the acoustic driver is 1 cm. One of the reasons for selecting this distance is that at

closer distances the acoustic driver blocks the rising vapor from advecting away from the vicinity of the heated surface, resulting in the formation of a vapor bridge between the surface and the acoustic driver which insulates the surface thereby severely limiting the CHF. Experiments are performed where the separation distance is varied and the CHF is determined without acoustic actuation. As reported earlier, when the separation distance is 1 cm, the unactuated CHF is 333 W/cm^2. This is only insignificantly different from the CHF measured when the acoustic driver is completely removed from the experiment (i.e., an infinite separation distance). By decreasing the separation distance to 5 mm the unactuated heat flux is decreased to 227 W/cm^2. And, by further decreasing the separation distance to 3.5 mm, the unactuated CHF is only 137 W/cm^2.

At separation distances less than 1 cm, the improvement due to the acoustic enhancement is increased significantly in terms of percentage improvement. At a separation distance of 5 mm, the CHF with a 1 kHz, 70.5 kPa acoustic field is 368 W/cm^2. Although this is 36 W/cm^2 less than the CHF under the same conditions for a 1 cm separation distance, it is an increase of 62% over the 227 W/cm^2 measured without the acoustic field and a separation distance of 5 mm. At a separation distance of 3.5 mm, the increase is even more dramatic. The CHF with a 1 kHz, 70.5 kPa acoustic field is 338 W/cm^2, which is a 147% improvement over the same case without an acoustic field! The critical heat fluxes and improvements at different separation distances are summarized in Table 1. These improvements could prove beneficial when space or other engineering requirements require a wall to be placed very near a heated surface cooled by two-phase boiling heat transfer.

Table 1. Comparison of natural and acoustically enhanced critical heat fluxes at different separation distances.

Separation Distance (mm)	q''_{CHF} (W/cm^2) No Acoustic Field ($T_S - T_{SAT}$)	q''_{CHF} (W/cm^2) 1 kHz, 70.5 kPa Acoustic Field ($T_S - T_{SAT}$)	Improvement
∞	333 (40.1°C)	N/A	N/A
10	333 (40.1°C)	404 (49.7°C)	21%
5	227 (38.4°C)	368 (28.7°C)	62%
3.5	165 (26.1°C)	338 (32.4°C)	147%

6.4 Corrections to the Measured Critical Heat Flux

The present work has shown that acoustic actuation increases the critical heat flux and delays the transition to film boiling. Since the presence of an acoustic field enables a higher heat flux, more heat is absorbed by the bulk liquid, resulting in a higher temperature rise over the course of an experiment than without actuation. In Figure 33, the temperature of the bulk liquid at the CHF in the presence of acoustic enhancement is 86.8° or 6.6°C higher than the temperature of the bulk liquid when the CHF is reached without any actuation. As shown by Equation 9 (Section 2.1), a decrease in subcooling (i.e., an increase in the temperature of the bulk liquid) results in a decrease in the CHF. Therefore, the CHF measured with acoustic actuation is actually lower than what it would be at the same subcooling in the absence of the acoustic field. Therefore, the CHF corrected for subcooling temperature is determined using Equation 9

$$q''_{CHF,SUB} = q''_{CHF,SAT}\left(1+\frac{T_{SAT}-T_{SUB}}{T_S-T_{SAT}}\right). \tag{9}$$

where $q''_{CHF,SAT}$ is determined using T_{SUB} = 86.8°C and $q''_{CHF,SUB}$ = 404 W/cm^2. The resulting value represents the estimated CHF if the bulk water temperature had been equal to the saturation temperature. The CHF for T_{SUB} = 80.2°C is computed using the calculated $q''_{CHF,SAT}$ to determine the new value for $q''_{CHF,SUB}$ at the lower bulk water temperature. These steps can be combined into a single equation

$$q''_{CHF,SUB}\Big|_{T_{SUB}=80.2°C} = q''_{CHF,SUB}\Big|_{T_{SUB}=86.8°C}\left(\frac{T_S - 80.2°C}{T_S - 86.8°C}\right) \tag{22}$$

which results in $q''_{CHF,SUB}$ = 446 W/cm^2 at T_{SUB} = 80.2°C. Thus, acoustic actuation would have increased the CHF by 34% at T_{SUB} = 80.2°C if the bulk liquid temperature had been kept constant.

Tillery (2004) and Sellers (2000) used a similar heater and discussed the measurement error of the heat flux due to the effect of the holes drilled into the heater's core to accommodate the thermocouples (Figure 10). These holes cause a slight decrease in the cross-sectional area of the heater. This reduction leads to a small increase in heat flux. Detailed analysis by Tillery shows that, for the dimensions of the calibrated copper heater, the measured heat flux is 3.5% larger than the actual heat flux. Of course, this discrepancy applies whether the acoustic field is present or not, so the relative increase due to acoustic actuation is not affected.

CHAPTER 7

CONCLUSIONS

The present work investigates the efficacy of using a small, light-weight, low-power acoustic driver to enhance boiling heat transfer from a flat surface by facilitating the removal of vapor bubbles from the surface and suppressing the instabilities that lead to the transition to film boiling at the critical heat flux. The acoustic field produced by the driver induces interfacial instabilities that affect a bubble's contact line with the heated surface and result in bubble detachment. Once detached, the bubble is easily advected into the bulk liquid by acoustic or buoyant forces.

The effects of the acoustic field on single air and vapor bubbles are investigated in the presence of the acoustic field. Variables that affect the interfacial instabilities include the frequency and sound pressure amplitude of the acoustic field and the bubble diameter. Next, the effect of the acoustic field on the boiling process on a submerged heater is studied and it was found that acoustic actuation increases the critical heat flux.

7.1 Acoustic Effects on a Single Air Bubble

The effects of the acoustic field on a single air bubble are investigated as a proof-of-concept demonstration of an acoustic field's ability to affect a gas bubble and to determine the important system variables. The air bubbles apparatus is designed to hold an air bubble of a determined size next to the underside of a horizontal, submerged surface using buoyancy so that the evolution of the bubble can be easily studied. It is found that within a range of acoustic frequencies, capillary waves are induced on the gas-

liquid interface of the air bubble. This frequency range depends on the size of the bubble. The amplitude of the capillary waves and the size of the frequency band are found to increase with sound pressure. When the sound pressure is sufficiently high, the actuation frequency can be tuned to force the capillary waves to a violent state that is enough to break the contact line and detach the bubble from the surface. Once detached, the bubble can easily be moved laterally along the surface by unbalanced forces (e.g. a weak convection current or an acoustic pressure). The time for acoustic detachment of an air bubble from the surface is about $1.2T_c$, where T_c is the characteristic time (determined by dividing the circumference of the bubble by the propagation speed of a capillary wave).

Fourier analysis of high speed video of an air bubble in the acoustic field is used to determine the frequencies of the capillary waves. At low capillary wave amplitudes, the power spectrum of the capillary waves has peaks at the frequency of the driving acoustic field, its subharmonic (strongest spectral peak), and multiples of the subharmonic suggesting that the capillary waves are Faraday waves. As the sound pressure amplitude increases, the amplitude of the capillary waves increases and the relative power at the driving frequency increases, while the other peaks began to broaden. When the amplitude of the capillary waves is sufficient to detach the bubble from the surface, the only dominant peak occurs at the driving frequency, while the rest of the spectrum becomes too noisy to distinguish individual peaks. The digital analysis also indicates that the acoustic field induces a radial oscillation of the bubble at the acoustic frequency. The radial oscillation of an air bubble with an equilibrium radius of 2.21 mm is about 0.055 mm, or 2.5%.

7.2 Acoustic Effects on a Single Vapor Bubble

The effects of the acoustic field on a single vapor bubble are investigated using a novel, planar boiling heat transfer surface designed to produce a single vapor bubble of a prescribed size. Capillary waves similar to the waves observed on the air bubble, are also induced on the interface the vapor bubble. Increasing the sound pressure amplitude and tuning the acoustic frequency within a range that depends on the bubble size increases the amplitude of the capillary waves until the vapor bubble is detached from the surface. The frequency at which the amplitude of the capillary waves is largest and is most likely to result in bubble detachment can be predicted using Equation 18 which shows the value of a dimensionless group including the frequency and bubble diameter to be constant.

After a vapor bubble is detached from the heated surface, it hovers on a thin layer of liquid near the surface due to the secondary Bjerknes force that overcomes the buoyancy force. Experiments show that the force is not a result of bulk fluid motion or acoustic streaming. The secondary Bjerknes force is typically thought of as the force between two oscillating gas bubbles in an acoustic field, but it also acts on a single oscillating bubble in the vicinity of a rigid wall. Estimates of the magnitudes of the Bjerknes and buoyant forces show that the secondary Bjerknes force (directed towards the surface) is larger than the sum of the primary Bjerknes force and the buoyant force (directed away from the surface).

7.3 Acoustically Enhanced Boiling

The present experiments demonstrate that acoustic forcing can increase the critical heat flux (CHF) during pool boiling over a submerged surface. In the present

setup, the CHF increases by 34% from 333 W/cm^2 (T_S - T_{SAT} = 40.1°C) to 446 W/cm^2 (T_S - T_{SAT} = 49.7°C) both with a 19.8°C subcooling. The acoustic field limits the formation of large vapor columns and delays transition from nucleate to film boiling. Acoustic enhancement is observed at frequencies between 0.7 and 1.2 kHz. The present frequency range is limited by the acoustic driver. Frequencies above 1.2 kHz are thought to be too high to adequately influence the vapor structures on a 1 cm^2 heater because these frequencies are outside the optimal frequency band for influencing the approximately 8 mm vapor structures that commonly occur. Preliminary experiments using a heater with a smaller exposed surface indicate that higher frequencies are effective on smaller heaters.

When the distance between the boiling surface and the 3.2 cm diameter driver is less than 1 cm, a vapor bridge forms between the two surfaces and results in a decrease of the CHF. At a separation distance of only 3.5 mm the natural CHF decreases to 165 W/cm^2. At the same separation distance, the acoustically enhanced CHF is 338 W/cm^2, which is a 147% improvement. Therefore, when a boiling surface is geometrically constrained, the acoustic enhancement can be beneficial in increasing the CHF.

7.4 Recommendations for Future Work

Future research on this technology should enhance the fundamental understanding of these phenomena by using high-resolution particle image velocimetry (PIV) to measure the flow around a bubble in the acoustic field. Special attention should be paid to the dynamics of the contact line that result in bubble detachment from the surface. In addition, greater understanding of the energy transfer mechanism from the time-

dependent pressure field to the gas-liquid interface of a bubble that induces capillary waves on the interface would help the understanding of why the acoustic field improves the CHF. An attempt should be made to derive expressions for the primary and secondary Bjerknes forces that include the effect of capillary surface waves on the bubble in the vicinity of a rigid wall. Better understanding of the relative magnitudes of the Bjerknes forces compared with the buoyancy force, and how the Bjerknes forces are dependent on system variables (acoustic frequency, sound pressure amplitude, etc.), will allow for optimization of the system to achieve maximum CHF improvement at the lowest driving power of the acoustic driver. The dependence of the physical phenomena on the fluid properties (density, surface tension, saturation temperature, etc.) and the atmospheric pressure should be determined by experimenting with fluids that have different boiling points and by changing the local ambient pressure. Decreasing the system pressure or the saturation temperature of the working fluid at atmospheric pressure would allow for boiling heat transfer to occur at lower system temperatures, possibly keeping the cooled electronic hardware cooler if similar heat fluxes are possible.

Another aspect of future work should be the development of a heat transfer module utilizing this technology to cool an actual electronic device. The ability of to dramatically increase the CHF at small separation distances will allow for the design of a compact module. Because the technology shows only an extension of the CHF (not an overall shift in the boiling curve), there is no need to operate the acoustic driver continuously. Instead, the driver should be turned on only when the heat flux (or the surface temperature) reaches a critical level. Activating the driver at this point will increase the CHF.

REFERENCES

Agostini, B., M. Fabbri, et al. (2007). "State of the Art of High Heat Flux Cooling Technologies." Heat Transfer Engineering **28**(4): 258-281.

Bar-Cohen, A. (1991). Thermal Management of Electronic Components with Dielectric Liquids. Proceedings of the 3rd ASME/JSME Thermal Engineering Joint Conference Part 2 (of 5), Reno, NV, USA.

Bar-Cohen, A. (1993). "Thermal Management of Electronic Components with Dielectric Liquids." JSME Int. J. **36**: 1-25.

Barbat, T., N. Ashgriz, et al. (1999). "Dynamics of Two Interacting Bubbles in an Acoustic Field." Journal of Fluid Mechanics **389**: 137-168.

Bjerknes, V. (1906). Fields of Force, Columbia University Press.

Bobrovich, G. I., I. I. Gogonin, et al. (1964). "Influence of Size of Heater Surface on the Peak Pool Boiling Heat Flux." Journal of Applied Mechanics and Technical Physics(No. 4): 137-138.

Crum, L. A. (1975). "Bjerknes Forces on a Bubble in a Stationary Sound Field." Journal of the Acoustical Society of America **57**(6.1): 1363-1370.

Das, A. K., P. K. Das, et al. (2006). "Heat Transfer During Pool Boiling Based on Evaporation from Micro and Macrolayer." International Journal of Heat and Mass Transfer **49**(19-20): 3487-3499.

Dhir, V. K. (1991). "Nucleate and Transition Boiling Heat Transfer under Pool and External Flow Conditions." International Journal of Heat and Fluid Flow **12**(4): 290-314.

Dhir, V. K. (1998). "Boiling Heat Transfer." Annual Review of Fluid Mechanics **30**: 365-401.

Dhir, V. K. (2001). "Numerical Simulations of Pool-Boiling Heat Transfer." AIChE Journal **47**(4): 813-834.

Dhir, V. K. (2006). "Mechanistic Prediction of Nucleate Boiling Heat Transfer-Achievable or a Hopeless Task?" Journal of Heat Transfer **128**(1): 1-12.

Eller, A. (1968). "Force on a Bubble in a Standing Acoustic Wave." Journal of the Acoustical Society of America **43**(1): 170-171.

Faraday, M. (1831). Philosophical Transactions of the Royal Society of London **121**: 319.

Fujita, Y. and S. Uchida (1998). "Enhancement of Nucleate Boiling on Composite Surfaces." Heat Transfer - Japanese Research **27**(3): 216-228.

Gaertner, R. F. (1965). "Photographic Study of Nucleate Pool Boiling on a Horizontal Surface." ASME Journal of Heat Transfer **87**: 17-29.

Gaertner, R. F. (1967). Method and Means for Increasing the Heat Transfer Coefficient between a Wall and Boiling Liquid. U. S. P. Office. United States.

Hao, Y., H. N. Oguz, et al. (2001). "The Action of Pressure-Radiation Forces on Pulsating Vapor Bubbles." Physics of Fluids **13**(5): 1167-1177.

Heffington, S. and A. Glezer (2004). Enhanced Boiling Heat Transfer by Submerged Ultrasonic Vibrations. Therminic. Sophia Antipolis, Cote d'Azur.

Heffington, S., S. Tillery, et al. (2003). Enhanced Boiling Heat Transfer by Submerged, Vibration Induced Jets. 9th International Workshop on Thermal Investigations of IC's and Systems, Aix-en-Provence, France, TIMA Lab.

Ho-Young, K., K. Yi Gu, et al. (2004). "Enhancement of Natural Convection and Pool Boiling Heat Transfer Via Ultrasonic Vibration." International Journal of Heat and Mass Transfer **47**(12-13): 2831-40.

Holt, R. G. and E. H. Trinh (1996). "Faraday Wave Turbulence on a Spherical Liquid Shell." Physical Review Letters **77**(7): 1274-7.

Hummel, R. L. (1965). Means for Increasing the Heat Transfer Coefficient between a Wall and Boiling Liquid. U. S. P. Office. United States of America.

Iida, Y. and K. Tsutsui (1992). "Effects of Ultrasonic Waves on Natural Convection, Nucleate Boiling and Film Boiling Heat Transfer from a Wire to a Saturated Liquid." Exp. Thermal Fluid Sci. **5**: 108-115.

Isakoff, S. E. (1956). Effect of an Ultrasonic Field on Boiling Heat Transfer -- Exploratory Investigation. Stanford, CA, Heat Transfer and Fluid Mechanics Institute. Stanford University Press**:** 15-28.

Jakob, M. (1949). Heat Transfer. New York, Wiley**:** 636-638.

Judd, R. L. and K. S. Hwang (1976). "Comprehensive Model for Nucleate Pool Boiling Heat Transfer Including Microlayer Evaporation." Journal of Heat Transfer, Transactions ASME **98 Ser C**(4): 623-629.

Kandlikar, S. G. (2001). "A Theoretical Model to Predict Pool Boiling Chf Incorporating Effects of Contact Angle and Orientation." ASME Journal of Heat Transfer **123**(6): 1071-1079.

Koster, J. N. and R. L. Sani, Eds. (1990). Low Gravity Fluid Dynamics and Transport Phenomena. Progress in Astronautics and Aeronautics. Washington DC.

Kutateladze, S. S. and L. L. Schneiderman (1953). Experimental Study of Influence of Temperature of Liquid on Change in the Rate of Boiling, USAEC Report**:** 95-100.

Leighton, T. G. (1994). The Acoustic Bubble. London, Academic Press Limited.

Liaw, S.-P. and V. K. Dhir (1986). Effect of Surface Wettability on Transition Boiling Heat Transfer from a Vertical Surface. Heat Transfer, Proceedings of the International Heat Transfer Conference, San Francisco, CA, USA, Hemisphere Publ Corp, Washington, DC, USA.

Liaw, S. P. and V. K. Dhir (1989). "Void Fraction Measurements During Saturated Pool Boiling of Water on Partially Wetted Vertical Surfaces." Journal of Heat Transfer, Transactions ASME **111**(3): 731-8.

Lienhard, J. H. (1970). Interacting Effects of Gravity and Size Upon the Peak and Minimum Pool Boiling Heat Fluxes, NASA**:** 87.

Lienhard, J. H. and V. K. Dhir (1973a). Extended Hydrodynamic Theory of the Peak and Minimum Pool Boiling Heat Fluxes, NASA Contractor Reports**:** 194.

Lienhard, J. H. and V. K. Dhir (1973b). "Hydrodynamic Prediction of Peak Pool-Boiling Heat Fluxes from Finite Bodies." Journal of Heat Transfer, Transactions ASME **95 Ser C**(2): 152-158.

Lienhard, J. H. and K. Watanbe (1965). On Correlating Peak and Minimum Boiling Heat Fluxes with Pressure and Heater Configuration. ASME Meeting HT-5.

Lighthill, J. (1978). Waves in Fluids. Cambridge, England, Cambridge University Press.

Ma, C. F. and A. E. Bergles (1983). Boiling Jet Impingement Cooling of Simulated Microelectronic Chips. Heat Transfer in Electronic Equipment. Presented at the Winter Annual Meeting of the ASME, Boston, Mass, USA.

Maracy, M. and R. H. S. Winterton (1988). "Hysteresis and Contact Angle Effects in Transition Pool Boiling of Water." International Journal of Heat and Mass Transfer **31**(7): 1443-9.

Markels, S. M., R. L. Durfee, et al. (1960). Annual Report of Methods to Increase Burnout Heat Transfer, Atomic Energy Commission.

Marsh, W. J. and I. Mudawar (1989). "Sensible Heating and Boiling Incipience in Free-Falling Dielectric Liquid Films." Transactions of the ASME. Journal of Electronic Packaging **111**(1): 46-53.

Mikic, B. B. and W. M. Rohsenow (1969). "A New Correlation of Pool-Boiling Data Including the Effect of Heating Surface Characteristics." Transactions of the ASME. Series C, Journal of Heat Transfer **91**(2): 245-50.

Monde, M. and Y. Katto (1978). "Burnout in a High Heat-Flux Boiling System with an Impinging Jet." International Journal of Heat and Mass Transfer **21**(3): 295-305.

Mudawar, I. (2000). Assessment of High-Heat-Flux Thermal Management Schemes. 7th Intersociety Conference on Thermal and Thermomechanical Phenomena in Electronic Systems-ITherm, Las Vegas, NV, USA, IEEE.

Mudawar, I. and T. M. Anderson (1989). High Flux Electronic Cooling by Means of Pool Boiling. Part I. Parametric Investigation of the Effects of Coolant Variation, Pressurization, Subcooling, and Surface Augmentation. National Heat Transfer Conference, Philadelphia, PA, USA, Publ by ASME, New York, NY, USA.

Mudawar, I. and D. E. Maddox (1989). Enhancement of Critical Heat Flux from High Power Microelectronic Heat Sources in a Flow Channel. National Heat Transfer Conference, Philadelphia, PA, USA, Publ by ASME, New York, NY, USA.

Nikolayev, V., D. Beysens, et al. (2006). "Bubble Spreading During the Boiling Crisis: Modelling and Experimenting in Microgravity." Microgravity Science and Technology **18**(3-4): 34-37.

Nikolayev, V. S., D. Chatain, et al. (2006). "Experimental Evidence of the Vapor Recoil Mechanism in the Boiling Crisis." Physical Review Letters, **97**(18): 184503.

Ornatskii, A. P. and V. K. Shcherbakov (1959). "Intensification of Heat Transfer in the Critical Region with the Aid of Ultrasonics." Teploenergetika **6**(1): 84-85.

Park, K. A. and A. E. Bergles (1988). "Ultrasonic Enhancement of Saturated and Subcooled Pool Boiling." International Journal of Heat and Mass Transfer **31**(3): 664-667.

Romie, R. E. and C. A. Aronson (1961). Adv. Tech. Lab. Rept. Atl-a-123.

Sellers, S. M. (2000). Heat Transfer Resulting from the Evaporation of Liquid Droplets on a Horizontal Heated Surface. Mechanical Engineering. Atlanta, GA, Georgia Institute of Technology. **Ph. D.:** 276.

Sheffield, R. J. (1994). High Heat Flux Spray Cooling. School of Mechanical Engineering. Atlanta, GA, Georgia Institute of Technology. **Ph. D.:** 182.

Sitter, J. S., T. J. Snyder, et al. (1998a). "Acoustic Field Interaction with a Boiling System under Terrestrial Gravity and Microgravity." **104**(5): 2561-9.

Sitter, J. S., T. J. Snyder, et al. (1998b). "Terrestrial and Microgravity Pool Boiling Heat Transfer from a Wire in an Acoustic Field." International Journal of Heat and Mass Transfer **41**(14): 2143-2155.

Straub, J. (2005). "Bubble - Bubbles - Boiling." Microgravity Science and Technology **16**(1): 242-248.

Takata, Y., S. Hidaka, et al. (2005). "Effect of Surface Wettability on Boiling and Evaporation." Energy **30**(2-4): 209-20.

Takata, Y., S. Hidaka, et al. (2003). "Pool Boiling on a Superhydrophilic Surface." International Journal of Energy Research **27**(2): 111-119.

Takata, Y., S. Hidaka, et al. (2006). "Boiling Feature on a Super Water-Repellent Surface." Heat Transfer Engineering **27**(8): 25-30.

Tillery, S. (2004). Enhanced Boiling Heat Transer by Submerged, Vibration Induced Jets. Mechanical Engineering. Atlanta, GA, Georgia Institute of Technology. **Master's of Science in Mechanical Engineering**.

Tillery, S. W., S. Heffington, et al. (2004). Boiling Heat Transfer Enhancement by Submerged, Vibration Induced Jets. ITherm 2004 - Ninth Intersociety Conference on Thermal and Thermomechanical Phenomena in Electronic Systems, Las Vegas, NV, United States, Institute of Electrical and Electronics Engineers Inc., Piscataway, United States.

Tillery, S. W., S. N. Heffington, et al. (2006). "Boiling Heat Transfer Enhancement Using a Submerged, Vibration-Induced Jet." Journal of Electronic Packaging **128**(2): 145-149.

Trinh, E. H., D. B. Thiessen, et al. (1998). "Driven and Freely Decaying Nonlinear Shape Oscillations of Drops and Bubbles Immersed in a Liquid: Experimental Results." Journal of Fluid Mechanics **364**: 253-272.

Wang, C. H. and V. K. Dhir (1993). "On the Gas Entrapment and Nucleation Site Density During Pool Boiling of Saturated Water." Journal of Heat Transfer, Transactions ASME **115**(3): 670-679.

Webb, R. L. (1981). "Evolution of Enhanced Surface Geometries for Nucleate Boiling." Heat Transfer Engineering **2**(3-4): 46-69.

Wen, M. Y. and C. Y. Ho (2003). "Pool Boiling Heat Transfer of Deionized and Degassed Water in Vertical/Horizontal V-Shaped Geometries." Heat and Mass Transfer **39**(8-9): 729-36.

Wong, S. W. and W. Y. Chon (1967). "Effects of Ultrasonic Vibrations on Burnout Heat Flux and Critical Temperature Difference." Can. J. Chem. Eng. **45**: 384-385.

Wong, S. W. and W. Y. Chon (1969). "Effects of Ultrasonic Vibrations on Heat Transfer to Liquids by Natural Convection and by Boiling." AIChE Journal **15**(2): 281-288.

Young, R. K. and R. L. Hummel (1965). "Improved Nucleate Boiling Heat Transfer." Chemical Engineering Progress Symposium Series **61**(59): 264-267.

Zerby, M. and M. Kuszewski (2002). Final Report on Next Generation Thermal Management (Ngtm) for Power Electronics, NSWCCD.

Zuber, N. (1957). "On Stability of Boiling Heat Transfer." ASME -- Paper: 4.